Progressive failure of ductile metals: Description via a three-dimensional coupled CZM-XFEM based approach

Konstantinos Nikolakopoulos, Jean-Philippe Crété, Patrice Longère

Progressive Failure Of Ductile Metals: Description Via A Three-dimensional Coupled CZM-XFEM Based Approach

Konstantinos Nikolakopoulos[a,b], Jean-Philippe Créte[b,*], Patrice Longère[a]

[a] *ISAE-SUPAERO, Université de Toulouse, ICA CNRS 5312, Toulouse, France*
[b] *SUPMECA, Laboratoire Quartz EA 7393, Saint-Ouen, France*

Abstract

The present work pertains to the numerical prediction of the current residual strength of large metallic engineering structures when submitted to accidental overloads. In this context, is developed a unified 3D numerical methodology reproducing the successive stages of the progressive failure of structures made of ductile metals, viz. (i) more or less diffuse micro-voiding induced damage, (ii) strain/damage localization in a narrow band, and (iii) macro-crack formation and propagation. This is notably realized via a combination of the GTN model and an XFEM/CZM coupling. Localization is addressed here as a phenomenon driven either by plastic instability or void coalescence. In the latter case an original transition criterion is proposed, accounting for the competition between Mode I/II type localization, utilizing the local triaxiality as a mode indicator. The methodology is implemented as a user element subroutine (UEL) within the commercial finite element computation code ABAQUS and its performance is assessed considering 3D numerical simulations of various loading cases. The proposed methodology is shown to be mesh objective and able to fairly reproduce ductile crack patterns, while it gives promising results regarding global specimen responses.

Key words: ductile damage, fracture, xfem, cohesive zone model, mode

*Corresponding author
Email address: jean-philippe.crete@supmeca.fr (Jean-Philippe Créte)

competition method

2020 MSC: 00-01, 99-00

Nomenclature

A_n	nucleation rate
A_{ii}	component for the calculation of the Linearization modulus
$\underset{\sim}{B}_1$, $\underset{\sim}{B}_2$	components for the calculation of the Linearization modulus
$\mathbf{B}$	spatial derivatives matrix of the shape functions
$\mathbf{B*}$	spatial derivatives matrix of the enriched shape functions
C_{loc}	cohesive tangent matrix
$\underset{\sim}{C}^e$	isotropic elastic stiffness tensor
$\mathrm{d}\alpha$	nodal displacement increments of the standard dofs
$\mathrm{d}\beta$	nodal displacement increments of the standard dofs
D	de-cohesion variable
D_c	critical value of the de-cohesion variable
E	Modulus of elasticity
f	Void volume fraction (porosity)
$\dot{f}$	porosity rate
$\dot{f}_g$	rate accounting for void growth
$\dot{f}_n$	rate accounting for void nucleation
f_0	initial porosity
f_c	critical porosity (porosity at void coalescence)
f_N	void volume fraction that can be ultimately nucleated
$f*$	porosity accounting for coalescence effects
$\mathbf{F}^{\alpha}_{ext}$	external forces corresponding to standard dofs
$\mathbf{F}^{\beta}_{ext}$	external forces corresponding to additional dofs
$\mathbf{F}^{\alpha}_{int}$	internal forces corresponding to standard dofs
$\mathbf{F}^{\beta}_{int}$	internal forces corresponding to additional dofs
$\boldsymbol{F_{coh}}$	cohesive forces

$\boldsymbol{F_{int}^0}$	internal forces at the time of localization
$\underline{g}$	vector tangent to the cohesive band plane
$\underline{g}_1$, $\underline{g}_2$	components of $\underline{g}$ on the band plane
$\underline{g}_{sh}$	vector tangent to the plane maximizing the shear stresses
G_c	energy release rate
$\underset{\sim}{G}_1$, $\underset{\sim}{G}_2$	components for the calculation of the Localization modulus
H	Heaviside function
H_j	value of the Heaviside function at node
I	number of nodes
$\underset{\sim}{I}$	identity tensor
J	number of enriched nodes
J_a	determinant of the Jacobian
k	strain hardening-related constant
k_s	function of T
$\mathbf{K}$	elements stiffness matrix
l_c	characteristic length
$\underset{\sim}{L}$	linearization modulus
M_{el}	mixicity factor
$nint$	number of Gauss points
$\underset{\sim}{n}$	plastic flow direction
$\underline{n}$	vector normal to the cohesive band plane
$\underline{n}_{ten}$	vector normal to the plane maximizing the tensile stresses
$\underline{n}_{sh}$	vector normal to the plane maximizing the shear stresses
N_i, N_j	i-th and j-th standard FE shape functions
p_m	hydrostatic pressure
p_m^e	trial equivalent stress
q_1, q_2	material constants
$\underset{\sim}{Q}$	acoustic tensor
R_0	initial size of the elasticity domain
R_∞	saturating value of strain hardening

$\mathbf{R}$	transformation matrix: global to local framework of the cohesive band
s_N	standard deviation
$\underset{\sim}{s}$	deviatoric part of the stress tensor
t_c	critical traction
$\underline{t}$	cohesive tractions vector
t^n, t^{g_1}, t^{g_2}	components of $\underline{t}$
$\underline{t}^*$	effective traction force vector
$\underline{t}_0$	traction force vector at cohesive band onset
$\underline{t}_{l1}$	vector collinear to the localization band front
$\underline{t}_{l2}$	vector normal to $\underline{t}_{l1}$
$Tr(\bullet)$	trace of a tensor
T	stress triaxiality
T_{sh}	critical local stress triaxiality value (shear)
T_{ten}	critical local stress triaxiality value (tension)
$\underline{u}$	displacement vector
$u(x)$	FE displacement field
$\boldsymbol{U}$	is the nodal displacements vector
V^e	finite element volume
V^-	element subvolume over discontinuity
V^+	element subvolume under discontinuity
w_i	weight of the Gauss point
α_i	i-th standard displacement degree of freedom
β_j	j-th additional degree of freedom associated to the j-th node
γ	power law exponential
Γ_D	discontinuity surface
δ_c	critical displacement
$\underline{\delta}$	displacement jump vector
δ_n, δ_1, δ_2	components of $\underline{\delta}$
δA	localization band surface increase
Δ	equivalent relative displacement

Δ_c	critical value of the equivalent relative displacement at complete fracture
$\Delta\epsilon^p$	plastic strain increment
$\Delta\epsilon_v$	volumetric part of the plastic strain increment
$\Delta\epsilon_d$	deviatoric part of the plastic strain increment
ΔH_α	evolution equations of the state variables
$\underset{\sim}{\epsilon}$	strain tensor
$\underset{\sim}{\epsilon}^e$	elastic strain tensor
$\underset{\sim}{\epsilon}^p$	plastic strain tensor
$\dot{\underset{\sim}{\epsilon}}$	strain rate tensor
$\dot{\underset{\sim}{\epsilon}}^e$	elastic strain rate tensor
$\dot{\underset{\sim}{\epsilon}}^p$	plastic strain rate tensor
$\dot{\epsilon}_v$	volumetric intensity
$\dot{\epsilon}_d$	deviatoric intensity
η	partial derivative of σ_y in terms of κ
κ	accumulated plastic strain
$\dot{\kappa}$	accumulated plastic strain rate
κ_N	the strain at the maximum micro-void nucleation rate
K	bulk modulus
$\dot{\Lambda}$	plastic multiplier
μ	elastic shear modulus
ν	Poisson's ratio
$\underline{\xi_i}$	vector containing the local coordinates of the Gauss point
ρ	a quantity to be integrated
$\underset{\sim}{\sigma}$	stress tensor
$\dot{\underset{\sim}{\sigma}}$	stress rate tensor
σ_{eq}	the equivalent stress
σ^e_{eq}	trial equivalent mean pressure
σ_{max}	maximum tensile stress
σ_y	yield stress
τ_{max}	maximum shear stress

$(\hat{\phi}, \hat{\theta})$	angle couple characterizing $\underline{n}$
$(\hat{\phi}_{ten}, \hat{\theta}_{ten})$	angle couple characterizing $\underline{n}_{ten}$
$(\hat{\phi}_{sh}, \hat{\theta}_{sh})$	angle couple characterizing $\underline{n}_{sh}$
Φ	plastic flow potential
Ψ	incremental function
ω	shear ratio
CDM	Continuum Damage Method
CZM	Cohesive Zone Method (Modelling)
dof	degree of freedom
FE	Finite Element
FEM	Finite Element Method
GP	Gauss point
GTN	Gurson - Tvergaard - Needleman model
ID	FE identity number
UEL	Abaqus User Elemennt
VAI	Volume Averaging Integration scheme
XFEM	eXtended Finite Element Method

1. Introduction

The objective of this work is the development of a unified three-dimensional methodology able to reproduce qualitatively and quantitatively, the successive stages of the progressive ductile failure, in the context of engineering design using commercial finite element computation codes. It is generally accepted that ductile cracks appear within a material following a three-stage process after plastic flow initiation: (i) more or less diffuse micro-voiding induced damage, (ii) strain/damage localization in a narrow band, and (iii) macro-crack formation and propagation. As soon as the loaded material is no longer able to accommodate the deformation by the sole plasticity, micro-voids nucleate (by particle/matrix debonding, phases separation, etc) and grow. At a more or less advanced stage of the loading, micro-voids coalesce and form narrow

bands wherein strain progressively localizes and meso-cracks nucleate. At the ultimate stage of the loading, meso-cracks coalescence themselves to form the traction-free macro-crack. The above mentioned stages are depicted in Fig. 1.

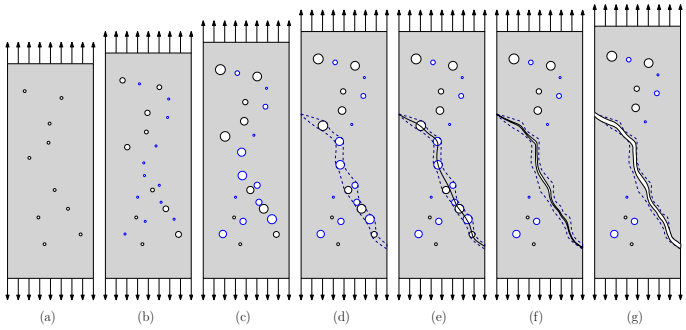

Figure 1: Ductile fracture process: (a) initial porosity, (b) and (c) void growth and nucleation, (d) appearance of a damage localization band, (e) and (f) void coalescence and meso-crack initiation, band material degradation, (g) macro-cracking

Since the development of continuum damage mechanics (CDM) by Kachanov[1], a great variety of models has been proposed to account for the coupling between elasticity/plasticity and micro-damage in ductile materials. One can notably cite the models by Lemaître [2], Perzyna [3] and Rousselier [4], while the most widely used undoubtedly remains the model by Gurson [5] as extended by Tvergaard and Needleman [6], known as the GTN model.

Many modified GTN models have been also proposed in order to take into account different loading conditions [7–10], matrix material behaviours [11, 12] or void shapes [13–15]. Yet, in the softening regime when employing the standard finite element method (FEM), the above mentioned CDM-based models exhibit a pathological mesh dependence as the result of the ill-posed problem. Among the methods aiming at regularizing the numerical solution, one can cite (integral and differential) non local models. They however require a very fine meshing and involve a characteristic length l_c [16, 17], a quantity that is not physical but rather numerically determined. Moreover, as a consequence of the fine meshing, these methods suffer from a high computational cost and increased complexity for distributed computing implementations [18].

Intrinsically, CDM is limited to phenomena preserving the continuity of the matter and must accordingly be replaced by other methods as soon as the crack-induced strong discontinuity is forming. The most widely used technique in FEM, due to its relative ease of implementation, is element deletion [19] or erosion [20, 21], the former rending nill the element strength while preserving the mass whereas the latter suppressing the element and involving a mass loss. Their inconvenience is that they induce a mesh dependency of the numerical results in terms of size and orientation. Full geometry remeshing [22, 23] or local mesh refinement [24] of highly damaged regions is often utilized to accommodate newly formed cracks in a meshed structure. They can be coupled to element erosion [25, 26], alleviating the mesh dependency issues or to the cohesive zone method (CZM) inserting cohesive elements in the newly formed interfaces [27]. They are also expensive in terms of computation time.

An alternative approach to methods based on the standard FEM has been the enriching of the kinematics of the FE formulation [28, 29]. The method that mostly captured the attention of the community has been the XFEM [30]. Its appeal consists in that there is no need for a priori knowledge of the crack path or remeshing as the crack is described via the node enrichment independently of the mesh. It has found application mostly on brittle fracture problems [31–33] but gives promising results regarding ductile failure simulation [16, 34, 35]. Nevertheless, in these cases the passage is realized directly from the diffuse damage state to the crack opening, neglecting the localization phase. Since damage localization implies gradual material degradation an interesting idea has been the coupling of the XFEM to CZM [36–40]. This way the softening process is better captured while avoiding abrupt load drops.

In the context of numerical simulation-aided engineering design, employing commercial finite element computation code, like Abaqus, the following requirements need to be met: (i) no alteration of the mesh connectivity mid-analysis, (ii) no a priori knowledge of the crack path, (iii) need for mesh objective results, using particularly coarse meshes, (iv) reasonable computational cost and simulation times, (v) straightforward implementation for the use of the practising

engineer. Taking these into consideration the use of the GTN model with an XFEM/CZM coupling appears as the most suitable choice both from a physical and a purely engineering perspective. The unified three-dimensional numerical methodology developed in the present work is schematically illustrated for one 3D finite element in Fig.2.

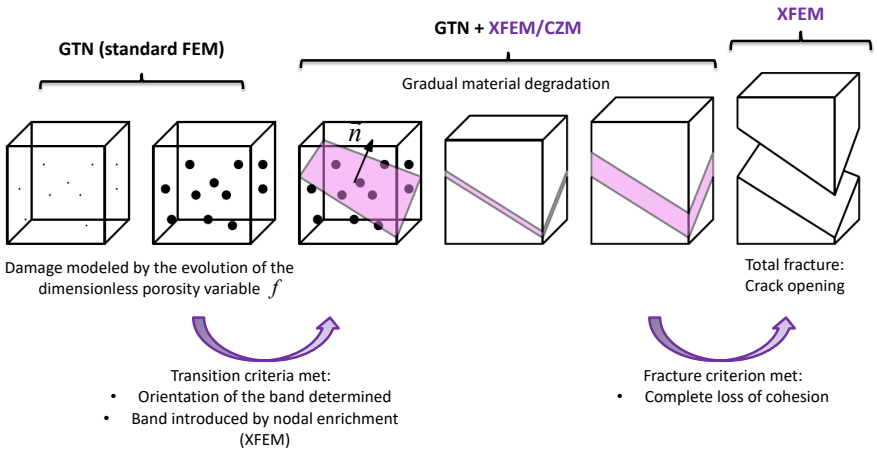

Figure 2: Unified numerical 3D methodology - one element example

Attention is paid to the development of transition criteria between the different stages, with particular interest in the description of Mode I vs Mode II type localization. The Mode competition and Mode transition is studied, especially in the aim of reproducing the 'cup and cone' effect in axisymmetric specimens under tension loading. Band propagation criteria are notably developed, which is generally rare for the 3D case [18].

In Section 2 the basic assumptions regarding the material model, the cohesive law and the adopted kinematic enrichment approach are outlined. The numerical three-dimensional operational method developed in this work, notably comprising criteria for element localization, band orientation, propagation and continuity, as well as the XFEM/CZM coupling formulation and the employed integration scheme, is described in Section 3. Finally, in Section 4 the unified

methodology is applied as an ABAQUS user element in 3D numerical simulations of various quasi-static loading cases and a study regarding the influence of the user defined parameters of the analysis is presented.

2. Preliminary considerations

In this section are presented some preliminary considerations regarding the damage-plasticity model, the cohesive law and the XFEM kinematics used in the present work.

2.1. Kinematic framework

Since ductile fracture is a phenomenon that potentially involves large strain and rotation, the finite strain framework would be required. However, the implementation of the unified methodology (GTN+XFEM/CZM) accounting for large deformation is considered an important challenge in itself. The choice of the adequate reference configuration and related strain and stress measures, associated to the computation of the internal forces and stiffness matrix and the need for ensuring the continuity of the band/crack in the current configuration, are all open. The main challenge involved in a formulation accounting for large strain and rotation is linked to the tracking of the propagating meso and macro-crack which is far more complex when the structure undergoes large rotations. A question that arises is whether the tracking of the meso and macro-crack should be realized relative to the initial or the current configuration (Lagrangian vs. Eulerian perspective, and their combination). For example Kumar et al.,[41] have adopted an updated Lagrangian approach to describe cracking in an elasto-plastic material without damage using 2D XFEM, Broumand and Khoei,[42] also adopted an updated Lagrangian approach in the framework of 2D XFEM, using a non-local damage-plasticity model, while, on the other hand, Legrain et al.,[43] argue that to deal with the problems of cracking within the XFEM framework in large deformations, the total Lagrangian approach is much more suitable. The numerous non-linearities of the model (GTN +

XFEM/CZM) do not facilitate the passage to large deformations, particularly affecting the convergence speed and the accuracy of the results. To the authors' knowledge, there are, currently, no models implemented in a commercial FE code that make use of an XFEM/CZM combination within the framework of ductile fracture in finite strain. For these reasons, in this work, efforts were concentrated on the development of a robust and reliable model making it possible to treat the ductile fracture of materials, albeit in the small strain framework, and the confrontation of various scientific challenges, e.g. the passage to 3D, the development of an efficient numerical integration scheme, physically motivated localization scenario and band propagation criteria. The present model can, thus, act as a reliable support for the passage to the large strain framework in the future.

In the small strain framework the strain tensor $\underset{\sim}{\epsilon}$ is defined by:

$$\underset{\sim}{\epsilon} = \frac{1}{2}((\nabla \underline{u}) + (\nabla \underline{u})^T) \tag{1}$$

where $\nabla \underline{u}$ is the displacement gradient. The total strain and total strain rate tensor can be accordingly decomposed into elastic and plastic contributions:

$$\underset{\sim}{\epsilon} = \underset{\sim}{\epsilon}^e + \underset{\sim}{\epsilon}^p \quad \text{and} \quad \dot{\underset{\sim}{\epsilon}} = \dot{\underset{\sim}{\epsilon}}^e + \dot{\underset{\sim}{\epsilon}}^p \tag{2}$$

where $\underset{\sim}{\epsilon}^e$ and $\underset{\sim}{\epsilon}^p$ represent the elastic and plastic strain tensors respectively. An overhead dot denotes the corresponding strain rate tensor.

2.1.1. Damage-plasticity model : GTN microporous plasticity model

The material under consideration is tentatively assumed to be rate and temperature independent. Here the coupling between plasticity and ductile damage, see Fig.2 (left), in the stage of more or less diffuse damage is described using the Gurson model [5] as modified by Tveergard and Needleman [6], taking into account isotropic hardening as well as void nucleation and growth induced softening. The GTN plastic flow potential is written as follows:

$$\Phi = \left(\frac{\sigma_{eq}}{\sigma_y}\right)^2 + 2q_1 f \cosh\left(-\frac{3}{2}q_2\frac{p_m}{\sigma_y}\right) - [1 + (q_1 f)^2] = 0 \tag{3}$$

with σ_{eq} the equivalent stress, $p_m = -\sigma_m$ the hydrostatic pressure, σ_y the yield stress, f the void volume fraction and q_1, q_2 material constants. The equivalent stress and pressure read:

$$\sigma_{eq} = \sqrt{\frac{3}{2}\underset{\sim}{s} : \underset{\sim}{s}} \quad \text{and} \quad p_m = -\frac{Tr(\underset{\sim}{\sigma})}{3} \tag{4}$$

where the deviatoric part $\underset{\sim}{s}$ of the stress tensor $\underset{\sim}{\sigma}$ is:

$$\underset{\sim}{s} = \underset{\sim}{\sigma} - \frac{1}{3}Tr(\underset{\sim}{\sigma})\,\underset{\sim}{I} \tag{5}$$

With $\underset{\sim}{\sigma}$ the Cauchy stress tensor, $\underset{\sim}{I}$ the identity tensor and $Tr(\bullet)$ the trace of a tensor. The yield stress σ_y accounting for isotropic strain hardening is assumed to obey a Voce type law:

$$\sigma_y = R_0 + R_\infty[1 - exp(-k\kappa)] \tag{6}$$

where R_0 the initial size of the elasticity domain, R_∞ the saturating value of strain hardening - $(R_0 + R_\infty)$ representing accordingly the maximum size of the elasticity domain -, k a strain hardening-related constant, and κ the accumulated plastic strain.

The instantaneous plastic strain rate is decomposed into a volumetric and a deviatoric contribution:

$$\underset{\sim}{\dot{\epsilon}}^p = \frac{1}{3}\dot{\epsilon}_v\underset{\sim}{I} + \dot{\epsilon}_d\underset{\sim}{n} \tag{7}$$

where $\dot{\epsilon}_v$ is the volumetric intensity and $\dot{\epsilon}_d$ is the deviatoric intensity and $\underset{\sim}{n} = \frac{3}{2}\frac{\underset{\sim}{s}}{\sigma_{eq}}$ the plastic flow direction. According to the normality rule, the expressions for the volumetric and deviatoric plastic strain rates are given respectively as:

$$\dot{\epsilon}_v = -\dot{\Lambda}\frac{\partial\Phi}{\partial p_m} \quad \text{and} \quad \dot{\epsilon}_d = \dot{\Lambda}\frac{\partial\Phi}{\partial\sigma_{eq}} \tag{8}$$

where $\dot{\Lambda}$ is the plastic multiplier.

The rate of the accumulated plastic strain κ is given in Gurson [5] as:

$$\dot{\kappa} = \frac{\sigma_{eq}\dot{\epsilon}_d - p_m\dot{\epsilon}_v}{(1-f)\sigma_y} \tag{9}$$

The porosity rate $\dot{f}$ is decomposed into two parts, $\dot{f}_g$ accounting for void growth and $\dot{f}_n$ for void nucleation:

$$\dot{f} = \dot{f}_g + \dot{f}_n \tag{10}$$

where $\dot{f}_g = (1-f)\dot{\epsilon}_v$, $f(0) = f_0$ and $\dot{f}_n = A_n\dot{\kappa}$

where the nucleation rate A_n is expressed as a Gaussian function [44]

$$A_n = \frac{f_N}{s_N\sqrt{2\pi}} exp\Big(-\frac{1}{2}\big(\frac{\kappa - \kappa_N}{s_N}\big)^2 \Big) \tag{11}$$

with f_N the void volume fraction that can be ultimately nucleated, κ_N the strain at the maximum micro-void nucleation rate and s_N the standard deviation.

There are some well-known limitations inherent to GTN model, e.g. the assumption of very small void volume fraction, its incapacity to describe the coalescence band induced plastic anisotropy, and the pathological mesh dependence in the softening regime and further uncontrolled numerical localization, amplified by the use of the erosion technique to describe the crack. In order to palliate these limitations, in this work, the kinematical consequences of the presence of a localization band are accounted for by the XFEM, while the band's physical consequences, i.e. softening due to material mechanical degradation, are phenomenologically reproduced by means of the cohesive law. The combination of the GTN model with an XFEM/CZM approach leads to a physic-numerical solution that is mesh objective, unlike other methods seeking to reproduce: void coalescence, via e.g. a micro-voiding amplification phenomenological function $f^*(f)$ as in Tvergaard and Needleman [6], or localization induced cracking, e.g. by means of the use of the element deletion technique.

2.1.2. Cohesive zone model (CZM)

The stage of diffuse damage growth is succeeded by the coalescence of voids in a thin localization band, see Fig.2 (center), wherein the progressive matter decohesion leading to the ultimate crack formation is accompanied by a gradual thermomechanical properties degradation leading to a complete loss of resistance. This phase can be phenomenologically described via the use of a

cohesive zone model. CZM is based on the early works of Dugdale [45], Barenblat [46, 47] and Hillerborg [48] and describes the progressive loss of cohesion via the use of a predetermined traction/separation relationship. One can typically distinguish two types of cohesive entities described by cohesive laws: 1) pre-existing cohesive entities having their own properties, such as structural adhesives between two parts or interface between two plies in laminate composites (usually designated as intrinsic cohesive laws), e.g. [49] (see Fig.3(b)), 2) cohesive entities not existing initially but forming under certain conditions at an advanced stage of the deformation process, with properties identical to the matrix at its onset and diverging from them along the deformation process (usually designated as extrinsic cohesive laws), e.g. [50, 51], see Fig.3(a). An intrinsic cohesive law that possesses both a hardening and a softening branch would be out of the scope of this work because the cohesive law is activated in an element at the time of localization. Thus, only an extrinsic cohesive law can be used in this work. The cohesive law is accordingly characterized only by a softening regime function, as depicted in Fig.3(a). Depending on the works of different authors, the criteria for the loss of (initial) linearity (deterioration onset) and ultimate failure (complete de-cohesion) are expressed mostly as a combination of two material parameters, e.g. in terms of critical displacement δ_c and critical traction t_c [52, 53] or critical traction and energy release rate G_c [54]. Particular attention must be paid to ensure the stress continuity at the

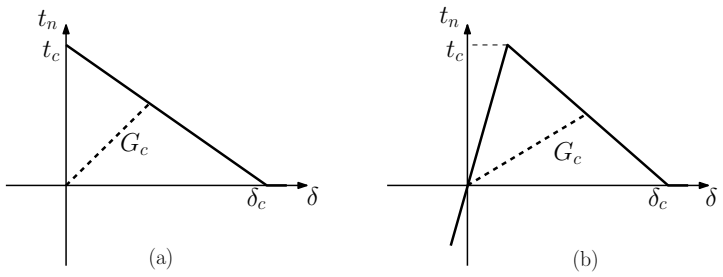

Figure 3: Extrinsic (a) and intrinsic (b) cohesive laws - Illustration of the evolution of the normal traction component t_n

cohesive law onset. For example, the initial (maximum) traction can be either

a fixed value or a value that is determined in each element at the cohesive law activation as a function of the current stress state. The method via which the cohesive model is incorporated into the finite element formulation as well as the criteria that indicate the passage from the continuous to the discontinuous phase will be presented in Section 3. The issue of the cohesive law shape in the global softening response of various tensile specimens will be addressed in 4.5.1.

2.1.2.1. Cohesive law.

Taking into consideration a 3D element crossed by a cohesive band, Fig.4, one can distinguish two surface vectors:

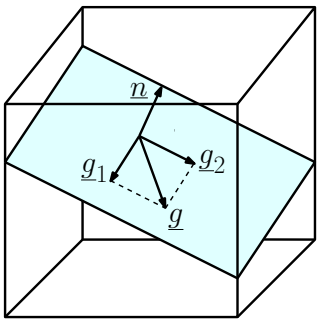

Figure 4: Finite element crossed by cohesive band

$\underline{n}$: vector normal to the cohesive band plane associated to the opening mode

$\underline{g}$: vector tangent to the cohesive band plane and collinear to the shear direction associated to the shearing mode that can be analysed into two components $\underline{g}_1$ and $\underline{g}_2$ on the band plane.

The $(\underline{n}, \underline{g}_1, \underline{g}_2)$ vector basis is orthonormal direct, meaning that the vectors are mutually perpendicular and of unit length.

The cohesive tractions $\underline{t}$ vector is the stress tensor $\underset{\sim}{\sigma}$ of the element projected on the cohesive band:

$$\underline{t} = \underset{\sim}{\sigma} \cdot \underline{n} = t^n \underline{n} + t^{g_1} \underline{g}_1 + t^{g_2} \underline{g}_2 = \{t^n, t^{g_1}, t^{g_2}\}_{(\underline{n}, \underline{g}_1, \underline{g}_2)} \tag{12}$$

with

$$t^n = \underline{n}^T \cdot \underline{\underline{\sigma}} \cdot \underline{n} \,, \quad t^{g1} = \underline{g}_1^T \cdot \underline{\underline{\sigma}} \cdot \underline{n} \quad \text{and} \quad t^{g2} = \underline{g}_2^T \cdot \underline{\underline{\sigma}} \cdot \underline{n} \tag{13}$$

The corresponding displacement jump vector reads

$$\underline{\delta} = \{\delta_n, \delta_1, \delta_2\}_{(\underline{n}, \underline{g}_1, \underline{g}_2)} \tag{14}$$

Instead of using different models for the opening and shearing modes, we are here tentatively considering a unique model expressed in terms of traction force vector $\underline{t}$ and equivalent relative displacement Δ:

$$\Delta = \sqrt{<< \delta_n >>^2 + \delta_1^2 + \delta_2^2} \tag{15}$$

Contact is treated indirectly, i.e. $<< \delta_n >>=\max(0, \delta_n)$, as a zero equivalent displacement jump when the normal component δ_n is negative (compression).

In addition, we are introducing the effective traction force vector as :

$$\underline{t}^* = \frac{\underline{t}}{(1-D)} \tag{16}$$

D in Eq.16 is a damage-like variable (evolving between 0 and 1) accounting for the progressive decohesion-induced material degradation along the deformation process. The rate independent cohesive model accordingly reads:

$$f(\underline{t}) = \underline{t}^* - \underline{t}_0 = \underline{0} \tag{17}$$

where $\underline{t}_0$ is the traction force vector at the cohesive band onset. It is noteworthy that $\underline{t}_0$ is not a priori postulated but results from the meeting of the band onset criterion and accordingly depends on the finite element considered, see Section 3.2.3. Inserting Eq.16 in 17, leads to :

$$f(\underline{t}) = \frac{\underline{t}}{(1-D)} - \underline{t}_0 = \underline{0} \tag{18}$$

Finally, the traction force vector is expressed as :

$$\underline{t} = (1-D)\underline{t}_0 \tag{19}$$

The manner in which each component of the tractions vector evolves can be seen in Fig.5.

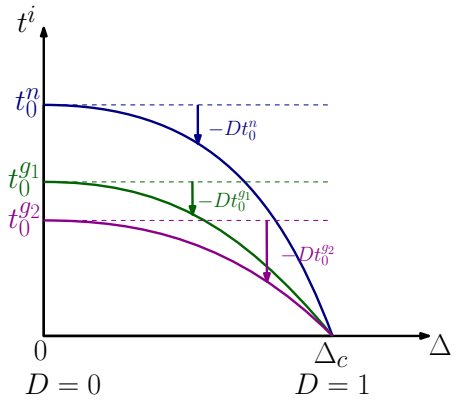

Figure 5: Evolution of the traction force components according to a cohesive 'power' law in 18 or 19

The evolution of the damage-like variable D takes a power law form:

$$D = \begin{cases} 0 & \text{if } \Delta \leqslant 0, \\ \left(\frac{\Delta}{\Delta_c}\right)^{\gamma} & \text{if } 0 < \Delta < \Delta_c, \\ 1 & \text{otherwise,} \end{cases} \tag{20}$$

where Δ_c is the critical value of the equivalent relative displacement at complete fracture ($D = 1$) of the element and the power law exponential $\gamma \geqslant 1$. While the complete loss of resistance of the band material requires $D = 1$, for numerical or physical reason a lower critical value D_c may be needed, viz. $D_c < 1$. As soon as the critical value of the decohesion variable D is reached the cohesive tractions vanish, leading to a traction free crack. For example D_c can take values between 0 for purely brittle fracture to 1 for purely ductile; though it usually lies in the range $[0.2, 0.5]$ [34].

2.1.2.2. Tangent matrix.

According to 19, the tangent matrix of the cohesive law is computed as follows where the subscript loc refers to the local frame of the localization band:

$$C_{loc}(i,j) = \frac{\partial t^i}{\partial \delta_j} = -\frac{\partial D}{\partial \delta_j} t_0^i = -\frac{\partial D}{\partial \Delta}\frac{\partial \Delta}{\partial \delta_j} t_0^i = -\frac{\gamma}{\Delta_c}\left(\frac{\Delta}{\Delta_c}\right)^{\gamma-1}\frac{\delta_j}{\Delta} t_0^i \tag{21}$$

with t_0^i the components of the initial tractions at the occurrence of localization in the element, calculated from the internal forces of the element in that instance (see Section 3.2.3) and $C_{loc}(i,1) = 0$ if $\delta_n < 0$ (compression).

Accordingly, the softening response of the material is fully characterized by three independent constant quantities, i.e. Δ_c, γ and D_c. The decision behind the use of such a cohesive law lies on its ability to reproduce a large number of different macroscopic behaviours by modifying a limited number of constant values.

2.2. Kinematic enrichment - Adopted X-FEM formulation

In the framework of the eXtended Finite Element Method the regular displacement field of the finite element u_{reg} is enriched by a discontinuous part u_{dis} to simulate the crack displacement jump following the work of Crété [35]. Another assumption in this paper is the 'shifted basis' formulation [55] wherein the discontinuous enrichment disappears at the element nodes. This way there is no need for transition elements. The displacement field is consequently described via the following relation:

$$u(x) = u_{reg} + u_{dis} = \sum_{i \in I} N_i \alpha_i + \sum_{j \in J} (H(x) - H_j) N_j \beta_j, \quad \text{where} \quad H_j = \pm 0.5 \quad (22)$$

where N_i, N_j is the i-th and j-th standard FE shape functions, I the number of nodes, α_i the i-th standard displacement degree of freedom, J the number of enriched nodes and β_j the j-th additional degree of freedom associated to the j-th node. H is the Heaviside function, which equals to +0.5 if a point is located at the 'positive' side of the discontinuity and -0.5 else and H_j the value of the Heaviside function at each node. In Fig.6 the reader can see the form of the shape functions in the case of a simple 1D element with a discontinuity in its middle point, before the application of the 'shifted basis' formulation (left) and after (right).

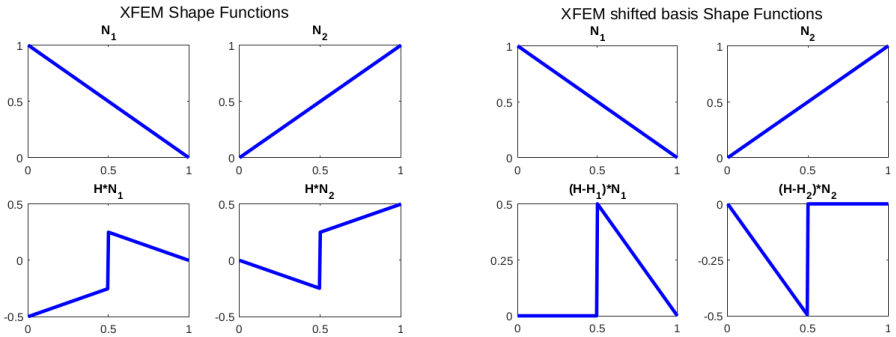

Figure 6: Example of shape functions for a 1D element with a discontinuity in its middle point - XFEM (left) and XFEM shifted basis (right)

3. Developed three-dimensional operational method

This Section aims at describing the unified numerical methodology developped to reproduce the successive stages sketched in Fig.2. A particular attention is paid to the intermediate stage of localization which is crucial for a better description of ductile failure. The transition criteria from diffuse damage to localization and from localization to fracture, as well as the band propagation criteria are discussed. The algorithms concerning localization onset and propagation, as well as the ABAQUS user element global algorithm are also presented.

The three-dimensional finite element (FE) used in the present approach is depicted in Fig.7. It contains 8 integration points (or Gauss points) for the calculation of the integrals associated with the stiffness matrix and internal forces vector, and an extra point at the FE centre participating only in the calculations concerning the localization criteria.

3.1. Stage of (more or less) diffuse damage

In the first stage of the present methodology, plasticity and the evolution of damage in the element are governed by the GTN model, see Section 2.1.1, in the framework of standard FEM.

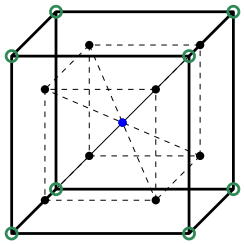

Figure 7: Specific 3D finite element developed in the present work

3.1.1. Integration of the constitutive rate equations

The numerical integration of the elasto-plastic equations is realized using the radial return procedure in combination with a Newton-Raphson algorithm, see Aravas [56] and Longère et al. [7]. By dividing Eq. 8.1 and 8.2 we eliminate the plastic multiplier and, expressing rates in an incremental form, we define a system of non-linear equations:

$$\begin{aligned}
\Psi = \Delta\epsilon_v \frac{\partial \Phi}{\partial \sigma_{eq}} + \Delta\epsilon_d \frac{\partial \Phi}{\partial p_m} = 0 \quad \text{(a)} \\
\Phi(\underset{\sim}{\sigma}, \sigma_{eq}; \kappa, f) = 0 \quad \text{(b)} \\
p_m = p_m^e + K\Delta\epsilon_v \quad \text{(c)} \\
\sigma_{eq} = \sigma_{eq}^e - 3\mu\Delta\epsilon_d \quad \text{(d)} \\
\Delta H_\alpha = h(\Delta\epsilon_v, \Delta\epsilon_d, p_m, \sigma_{eq}, \kappa, f) \quad \text{(e)}
\end{aligned} \tag{23}$$

where p_m^e, σ_{eq}^e are the trial equivalent stress and mean pressure, μ and K the elastic shear and bulk moduli and ΔH_α a system of equations of the state variables, see [56].

3.1.2. Linearization modulus

In order for the finite element code to solve the equilibrium at a given increment one needs to determine the linearization modulus $\underset{\sim}{L}$, the latter provides the code with the variation of the stress increment due to a variation in the strain increment, consistent with the algorithm used for the numerical integra-

tion, in this case implicit time integration. The linearization modulus must not be confused with the elasto-plastic tangent operator. For more information on this implementation the reader can refer to Aravas [56].

The linearization modulus is derived from:

$$\partial \underset{\sim}{\sigma}_{t+\Delta t} = \underset{\sim}{\underset{\sim}{L}} : \partial \underset{\sim}{\epsilon}_{t+\Delta t} \tag{24}$$

The elasticity equation gives:

$$\underset{\sim}{\sigma}_{t+\Delta t} = \underset{\sim}{\underset{\sim}{C}}^{e} : \underset{\sim}{\epsilon}^{e}_{t+\Delta t} = \underset{\sim}{\underset{\sim}{C}}^{e} : \left[\underset{\sim}{\epsilon}_{t+\Delta t} - \left(\underset{\sim}{\epsilon}^{p}_{t} + \Delta \epsilon^{p}\right)\right] =$$

$$\underset{\sim}{\underset{\sim}{C}}^{e} : \left(\underset{\sim}{\epsilon}_{t+\Delta t} - \underset{\sim}{\epsilon}^{p}_{t} - \frac{1}{3}\Delta\epsilon_v \underset{\sim}{I} - \Delta\epsilon_d \underset{\sim}{n}\right) \tag{25}$$

Hence,

$$\partial \underset{\sim}{\sigma}_{t+\Delta t} = \underset{\sim}{\underset{\sim}{C}}^{e} : \left(\partial \underset{\sim}{\epsilon}_{t+\Delta t} - \frac{1}{3}\partial\Delta\epsilon_v \underset{\sim}{I} - \partial\Delta\epsilon_d \underset{\sim}{n} - \Delta\epsilon_d \frac{\partial \underset{\sim}{n}}{\partial \underset{\sim}{\sigma}_{t+\Delta t}} : \partial \underset{\sim}{\sigma}_{t+\Delta t}\right) \tag{26}$$

Where $\underset{\sim}{\underset{\sim}{C}}^{e}$ is the isotropic elastic stiffness tensor. Derivation of Eq. 23(a) and 23(b) leads to the following system of equations, then solving for $\partial\Delta\epsilon_v$ and $\partial\Delta\epsilon_d$:

$$\begin{bmatrix} A_{11} & A_{12} \\ A_{21} & A_{22} \end{bmatrix} \left\{ \begin{array}{c} \partial\Delta\epsilon_v \\ \partial\Delta\epsilon_d \end{array} \right\} = \left\{ \begin{array}{c} \underset{\sim}{B}_1 \\ \underset{\sim}{B}_2 \end{array} \right\} : \partial \underset{\sim}{\sigma}_{t+\Delta t} \tag{27}$$

hence, inverting 27

$$\left\{ \begin{array}{c} \partial\Delta\epsilon_v \\ \partial\Delta\epsilon_d \end{array} \right\} = [A]^{-1} \left\{ \begin{array}{c} \underset{\sim}{B}_1 \\ \underset{\sim}{B}_2 \end{array} \right\} : \partial \underset{\sim}{\sigma}_{t+\Delta t} = \left\{ \begin{array}{c} \underset{\sim}{G}_1 \\ \underset{\sim}{G}_2 \end{array} \right\} : \partial \underset{\sim}{\sigma}_{t+\Delta t} \tag{28}$$

The A_{ij}, B_i and G_i components are presented in the Appendix A. Injecting 28 into 26 yields:

$$(\underset{\sim}{I} + \underset{\sim}{\underset{\sim}{C}}^{e} : \underset{\sim}{\underset{\sim}{M}}) : \partial \underset{\sim}{\sigma}_{t+\Delta t} = \underset{\sim}{\underset{\sim}{C}}^{e} : \partial \underset{\sim}{\epsilon}_{t+\Delta t} \tag{29}$$

where

$$\underset{\sim}{\underset{\sim}{M}} = \frac{1}{3}\underset{\sim}{I} : \underset{\sim}{G}_1 + \underset{\sim}{n} : \underset{\sim}{G}_2 + \Delta\epsilon_d \frac{\partial \underset{\sim}{n}}{\partial \underset{\sim}{\sigma}_{t+\Delta t}} \tag{30}$$

Hence

$$\underset{\sim}{\underset{\sim}{L}} = \left(\frac{\partial \underset{\sim}{\sigma}}{\partial \underset{\sim}{\epsilon}}\right)_{t+\Delta t} = (\underset{\sim}{I} + \underset{\sim}{\underset{\sim}{C}}^{e} : \underset{\sim}{\underset{\sim}{M}})^{-1} : \underset{\sim}{\underset{\sim}{C}}^{e} \tag{31}$$

The symmetry of the operator is imposed for the reduction of the cost of the analysis and the improvement of the convergence [56]. The linearization modulus is finally expressed by:

$$\underset{\sim}{\underset{\sim}{L}} = \frac{1}{2}(\underset{\sim}{\underset{\sim}{L}} + \underset{\sim}{\underset{\sim}{L}}^T) \tag{32}$$

3.2. Stage of localization

3.2.1. From diffuse damage to localization

The conditions that trigger the passage from standard FEM to eXtended FEM, i.e. that activate the enrichment degrees of freedom, are twofold. First, the passage in the softening regime is indicated via a pre-localization indicator and, second, a distinction is made, see Fig.8 below and Fig.15 in Pineau et al.[57]: case (a) localization onset due to plastic instability, indicated by the satisfaction of the bifurcation criterion, followed by void coalescence within this band, case (b) standard void coalescence, indicated by a phenomenological criterion expressed in terms of critical porosity, leading to a damage localization band formation.

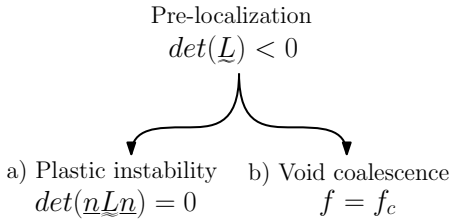

Figure 8: Illustration of the two localization cases

The need for such a two-case criterion arises from the observation that plastic instability is not always numerically detected even well inside the softening regime, e.g. [58]. In this work (a) and (b) case criteria are inspected sequentially (if needed) in each pre-localized element.

3.2.1.1. Pre-localization criterion.

In this work the condition for an element to be a potential candidate for localization (localizable) is derived from the Drucker's stability postulate, i.e.

the positiveness of the 2nd order work. The necessary condition for material stability proposed by Drucker [59] is that the work done externally is positive:

$$\dot{\underset{\sim}{\sigma}} : \dot{\underset{\sim}{\epsilon}} > 0 \tag{33}$$

Softening implies the occurrence of negative work. This coincides with the appearance of a negative eigenvalue of the tangent stiffness operator. This is to be expected as soon as negative eigenvalues signify energy release [60], a phenomenon involved in the creation of damage localization bands. Simply put, in this work an element is considered as a potential candidate for localization when negative work leading to softening is detected, i.e.:

$$det(\underset{\sim}{L}) < 0 \tag{34}$$

In the first case, mentioned in Section 3.2.1, all possible planes are probed as to whether they satisfy the bifurcation criterion in an element. In three-dimensions these calculations, if applied to all elements at every increment until localization onset, can become computationally cumbersome, especially for the modelling of large structures. The adopted pre-localization criterion is simple and easy to calculate so that the search of localized elements can be narrowed to a small number of potential candidates. Equivalently, in the second case, where localization is triggered by a critical porosity, the pre-localization criterion corroborates that the element has indeed entered the softening phase.

A finite element is said to meet the pre-localization criterion as soon as the condition 34 is satisfied in the central Gauss point, see Fig.7, in the finite element in question. The ID and the porosity f of all elements satisfying the pre-localization criterion, Eq.34, in each increment, are saved and then sorted by order of decreasing porosity in a matrix indicatively named `PreLocEle`[`ID`,f].

3.2.1.2. Localization criteria.

After the softening initiation indicator (Eq. 34) has manifested itself, we seek to determine whether the element will localize. All elements satisfying this

condition are introduced in a list and sorted with decreasing porosities. The localization criteria, presented below, are checked at the list elements with that order. The calculation of all quantities are done in a GP located in the element's centre (this GP does not participate in the calculation of the stiffness and internal force matrices, see Fig.7).

a) Case of plastic instability-induced localization

In the case of a rate-independent material the initiation of an instability induced strain localization band can be detected employing the bifurcation analysis [61]. In order to verify the existence of a band one needs to calculate the acoustic tensor $\underset{\sim}{Q} = \underline{n}\,\underset{\sim}{L}\,\underline{n}$, where $\underline{n}$ is the normal vector to the band and $\underset{\sim}{L}$ the linearization modulus 32. The bifurcation criterion reads:

$$det(\underset{\sim}{Q}) = 0 \tag{35}$$

When the acoustic tensor becomes singular, i.e. one of its eigenvalues and the determinant become zero, a localization band is indeed expected to appear, i.e. 35 is satisfied. Practically, these conditions are never exactly met, so the criterion evolves to finding the normal $\underline{n}$ for which $det(\underset{\sim}{Q}) < 0$ for the first time, while at the same time minimizing the acoustic tensor [61]:

$$min(det(\underset{\sim}{Q})) < 0 \tag{36}$$

For each angle $\hat{\phi} \in [0^o, 359^o]$ an angle $\hat{\theta} \in [0^o, 89^o]$ is scanned and a $\underline{n}$ vector is calculated for each combination. The normal vector of a surface can be characterized by two angles ($\hat{\phi}$, $\hat{\theta}$), see Fig.9, in the following sense:

$$\underline{n} = \left\{ \begin{array}{c} \cos\hat{\phi} \cdot \cos\hat{\theta} \\ \cos\hat{\phi} \cdot \sin\hat{\theta} \\ \sin\hat{\phi} \end{array} \right\} \tag{37}$$

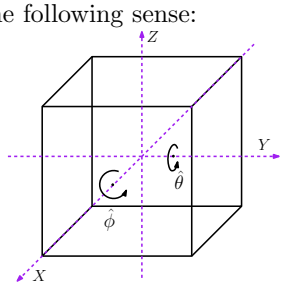

Figure 9: Illustration of the probing of $\hat{\phi}$ and $\hat{\theta}$ angles

The vector retained is the one that satisfies the bifurcation criterion 36.

b) Case of void coalescence-induced localization

Unlike the bifurcation criterion 35 or 36 that provides with both the band onset and the band orientation, two criteria are needed for void coalescence-induced localization, one for the band onset and another for the band orientation.

Onset criterion

When searching for conditions for coalescence onset, one can distinguish two main approaches: (i) a phenomenological approach, such as in Tvergaard and Needleman [6], where a critical porosity is used as a threshold from which the evolution of porosity is accelerated, and (ii) a numerical micromechanics based approach, e.g. Pardoen and Hutchinson [62, 63]. In this work the former criterion is employed as the most simple and practical one from an engineering point of view. This means that as porosity increases there is a point at which the void concentration is high enough for a distinct band of damage to be witnessed. Examples of f_c values in the literature are between 0.03 and 0.15 ([6, 11, 39]) in steel alloys, 0.035 in aluminium alloys [64]. However, it is not unusual to treat f_c as a function of the initial porosity f_0, e.g. [13, 65]. It is clear though that porosity at localization onset depends on the material under consideration.

The condition for void coalescence-induced localization accordingly reads

$$f = f_c \tag{38}$$

Band orientation

The critical porosity as a coalescence triggering criterion is not able in itself to provide us with the damage band orientation. In this work that information is derived from the stress state as there is a competition between Mode I and Mode II driven coalescence.

The first step of the present method is consequently the calculation of two candidate localization planes in the element that maximize the tensile and shear

stress, with normal vectors $\underline{n}_{ten}$ and $\underline{n}_{sh}$ respectively:

$$\begin{aligned} \sigma_{max} &= \underline{n}_{ten}^{T} \cdot \underset{\sim}{\sigma} \cdot \underline{n}_{ten} \\ \tau_{max} &= \underline{g}_{sh}^{T} \cdot \underset{\sim}{\sigma} \cdot \underline{n}_{sh} \text{ where } \underline{g}_{sh} \cdot \underline{n}_{sh} = 0 \end{aligned} \tag{39}$$

Numerically, in this case too, all possible planes are probed, i.e. for each angle $\hat{\phi} \in [0^o, 359^o]$ an angle $\hat{\theta} \in [0^o, 89^o]$ is scanned and the $\underline{n}_{ten}$ and $\underline{n}_{sh}$ are calculated.

The second step is the determination of a criterion that will discern between Mode I and Mode II type localization, allowing for selecting one between the two potential localization planes.

Some criteria for the transition between normal and shear stress dominated loading conditions have been proposed in the literature, though mostly applied to 2D problems, e.g. Sutton et al.[66], Liu et al.[67], Haboussa et al.[68]. In this work the stress triaxiality $T = \sigma_m/\sigma_{eq}$ is favoured as the Mode indicating quantity. That is because it can provide us with a better insight into the micro-scale mechanisms at play. Mode I dominated states generally involve pure void growth in high triaxialities, while Mode II dominated states implicate void distortions at lower triaxialities. Studying unit voided cells Kiran et al. [69] state that void shape change appears at triaxialities lower than 0.4 for ATSM A992 steels. On the other hand Liu et al. [70], also report pure void growth at high stress triaxialities and void distortions for low triaxialities. More importantly they describe the apparition of a transition zone that effectively separates the two mechanisms, which is determined at $0.43 < T < 0.52$. It is similarly mentioned in Bao and Wierzbicki [71] that fracture is possible to appear as a combination of two modes, for intermediate triaxialities. For this reason in this work it is considered that there is a region that Mode I and Mode II mechanisms are interacting leading to a Mode mixicity law. The adopted mixicity law in this work is inspired by the work of Haboussa et al. [68], also employed by Elguedj et al. [72].

Here the transition zone between Mode I and Mode II type localization is delimited by the local stress triaxiality values T_{sh} (denoting shear) and T_{ten}

(denoting tension). These values will be evaluated in Section 4.3.1.

The plane angle couples $(\hat{\phi}_{ten}, \hat{\theta}_{ten})$ and $(\hat{\phi}_{sh}, \hat{\theta}_{sh})$, corresponding to $\underline{n}_{ten}$ and $\underline{n}_{sh}$ respectively, are those that maximize the normal and the shear stress. The actual angles for an element whose local triaxiality state lies in the mixed-mode region is calculated as a weighted average of the two, see Fig.10:

$$\begin{aligned} \hat{\phi} &= M_{el}\,\hat{\phi}_{sh} + (1 - M_{el})\,\hat{\phi}_{ten} \\ \hat{\theta} &= M_{el}\,\hat{\theta}_{sh} + (1 - M_{el})\,\hat{\theta}_{ten} \end{aligned} \tag{40}$$

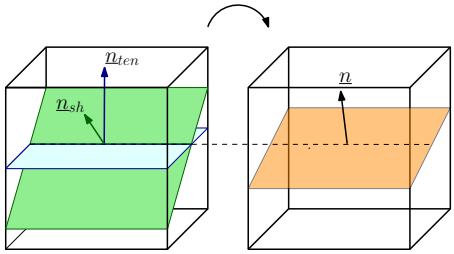

Figure 10: Illustration of localization plane as an average of the planes maximizing the normal and shear stresses

$$\text{where} \quad M_{el} = \frac{\omega}{1 - k_s T} \quad \text{the mixicity factor} \tag{41}$$

$$\text{with} \quad \omega = \frac{\tau_{max}}{\sigma_{eq}} \quad \text{and} \quad k_s = \frac{1}{exp(T)} \tag{42}$$

In 41 ω is a shear ratio, proposed in the work of Hooputra et al. [73] and is a measure of the influence of the maximum shear stress. In Fig. 11 the principle of the method for the determination of the angle $\hat{\theta}$ is shown. The same approach is applied also to angle $\hat{\phi}$.

A finite element is said to meet the localization criterion as soon as one of the two conditions 36 or 38 is satisfied in the central Gauss point in the finite element in question.

3.2.2. Localization band spatial representation

3.2.2.1. Initiation.

We are here considering several adjacent 8-Gauss point band-free finite ele-

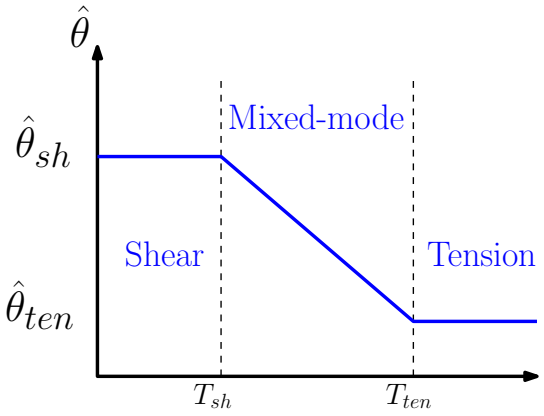

Figure 11: Band orientation angle as a function of the stress triaxiality ratio completing the void coalescence induced localisation onset $f = f_c$

ments (FE), as depicted in two-dimensions in Fig.12. We are distinguishing two cases that depend on the location of the FE, wherein a band is about to form with a given orientation, with respect to the boundary. For an about-to-localize FE situated on an outer free surface of the specimen, the band is introduced in the centre of the free side, Fig.12 (left). For an about-to-localize FE in the interior of the mesh, the band is introduced in the middle of the element, Fig.12 (right).

In the present methodology, the band can tentatively initiate in only one element and propagate to adjacent elements. On the other hand, the porosity in every Gauss point is frozen once it has reached the f_c value. Since coalescence and material degradation is treated by the cohesive law there is no need for the porosity to continue evolving.

3.2.2.2. Band Propagation & Continuity.

We are here considering 2 adjacent 8-Gauss point finite elements (FE), a first one designated m containing a localization band of normal $\underline{n}^{(m)}$, and a second one designated j containing no localization band, see Fig.13. The band front is thus the segment [AB] belonging to the side common to FEs m and j and collinear to $\underline{t}_{l1}^{(m)}$ (and of normal $\underline{t}_{l2}^{(m)} = \underline{n}^{(m)} \wedge \underline{t}_{l1}^{(m)}$, $\underline{t}_{l1}^{(m)}$ and $\underline{t}_{l2}^{(m)}$ being 2

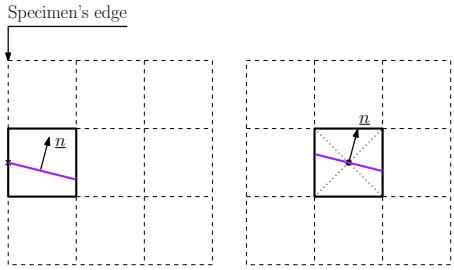

Figure 12: Placement of the band in the first localized element

vectors in the band plane in FE m), and is delimited by the points A and B belonging to 2 of the 4 edges of the side common to FEs m and j - the fact that A and B belong to 2 different edges is a constraint.

The continuity of the band between FEs m and j implies that the segment [AB] is common to the (already existing) band in m and (about to form) band in j, of normals $\underline{n}^{(m)}$ and $\underline{n}^{(j)}$, respectively. As a consequence, $\underline{t}_{l1}^{(j)} = \underline{t}_{l1}^{(m)}$ and $\underline{t}_{l1}^{(m)} \cdot \underline{n}^{(j)} = 0$, viz. the bases formed by the couples $(\underline{n}^{(m)}, \underline{t}_{l2}^{(m)})$ and $(\underline{n}^{(j)}, \underline{t}_{l2}^{(j)})$ define the same plane and are inclined by an angle ϕ covering the range $[-45^o, 45^o]$, see Fig.13.

The aim is now to find the angle ϕ satisfying one of the two localization criteria, viz. related to either plastic instability or void coalescence, see Section 3.2.1.2.

Beforehand, it is needed to account for certain conditions that artificially prevent the localization band to propagate. Such a situation is depicted in Fig.14 where the (red coloured) FE adjacent to the FE containing the band front meets the pre-localization criterion but does not meet a localization criterion, inhibiting further propagation of the band, whereas its (cyan coloured) neighbour does. To overcome this issue, it is necessary to realize a localization analysis not only in the closest neighbour but also in a group of neighbours contained in a patch (of radius R, perpendicular to the band front). The band orientation determined in the cyan coloured element in the patch is then applied to the red coloured element, respecting, at the same time, the band continuity.

Practically, this method is only applied in the localization case (a) when the bifurcation criterion is not satisfied.

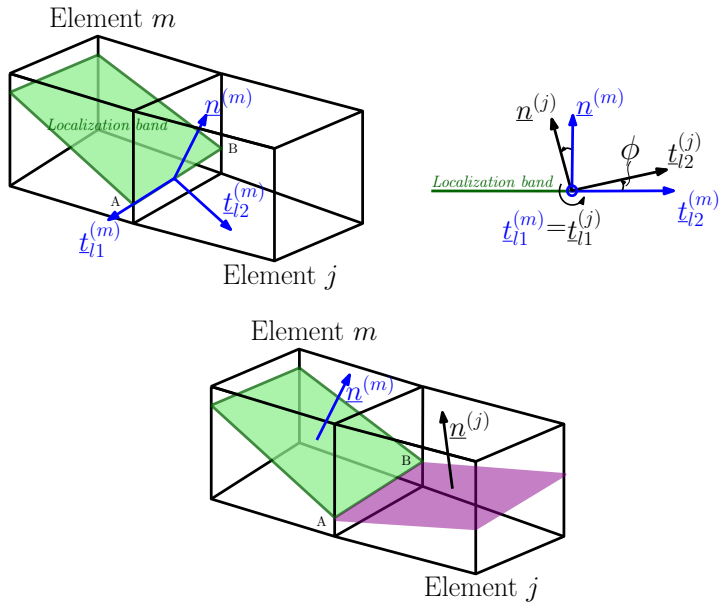

Figure 13: Band orientation for better continuity

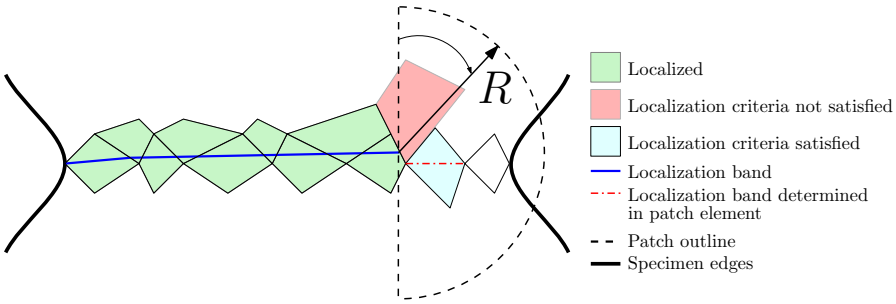

Figure 14: Hemispherical patch method - 2D example

Independently of any localization criterion, if 3 edges of element j are already 'cut' by other elements' bands (defining 3 intersection points) the j element's localization plane is the one passing through these three intersection points. The

vector normal to this plane is thus directly defined, as well as its corresponding $\hat{\phi}$ and $\hat{\theta}$ angles. This way band continuity is assured.

The algorithm for the band initiation and orientation is briefly presented in Algo. 1.

3.2.2.3. Band propagation conditions.

As in the approaches of Crété et al.[35] and Wolf et al.[39] the band propagation follows the concept of element exhaustion. The surface increase δA of the band is simply determined by checking certain criteria in all localizable elements; the band is introduced in elements that satisfy all the criteria in the same increment. The criteria are the following:

1. Elements must satisfy the pre-localization criterion ($det(\underset{\sim}{L}) < 0$).
2. Since multiple initiation sites are not treated in this work, elements must be connected to an already localized element and share a side.
3. The adjacent band must intersect this shared side.
4. Elements that satisfy 1, 2 and 3 are checked by order of decreasing porosity (using the `PreLocEle` matrix, see Sec.3.2.1) in a spiral mode around a localized element, see Fig. 15.
5. The elements satisfying at least one of the two localization criteria are localized.
6. Steps 1 to 5 are repeated until no element of the model is found to localize.
7. If the computation does not converge (10 successive time step reductions which do not converge) the propagation step which has just taken place is canceled.
8. If the time increment has reduced to less than 10^{-5} no propagation takes place.

The algorithm for the band propagation is briefly presented in Algo. 2.

Algorithm 1: Element localization & band orientation algorithm

if $det(\underset{\sim}{L}) > 0$ **then**;
  No localization;
else;
  if there are no other localized elements **then**;
    if $min(det(\underset{\sim}{Q})) < 0$ satisfied **then**;
      Element localized;
    else if $f \geqslant f_c$ **then** ;
      Mode competition criterion;
      Element localized;
    else no localization;
  else;
    if 3 edges already cut **then**;
      Element localized;
    else if $min(det(\underset{\sim}{Q})) < 0$ satisfied $\in [-45^o, 45^o]$ $\circlearrowleft$ band tip and 2 edges already cut **then**;
      Element localized;
    else if $min(det(\underset{\sim}{Q})) < 0$ satisfied in elm. of patch $\perp$ band tip and 2 edges already cut **then**;
      Element localized;
    else if $f \geqslant f_c$ and 2 edges already cut **then**;
      Mode competition criterion $\in [-45^o, 45^o]$ $\circlearrowleft$ band tip;
      Element localized;
    else No localization;
End loop - next element

Algorithm 2: Band propagation algorithm

Result: Band introduced to new elements

All localizable elements $[det(\underset{\sim}{L}) < 0]$ are inserted in a list;

List sorted with respect to porosity f ;

'Element localization algorithm' is applied to the element list ; `// with order of decreasing` f

1^{st} localized element ✓;

Check elements in a spiral around the localized element:;

- elements sharing a side with the localized element;

- the band intersects this shared side;

The elements satisfying the above criteria & the localization criteria are localized ; `// Element localization algorithm 1`

- Repeat loop: until all elements satisfying the criteria are exhausted.;

Enriched dofs activated;

Next increment

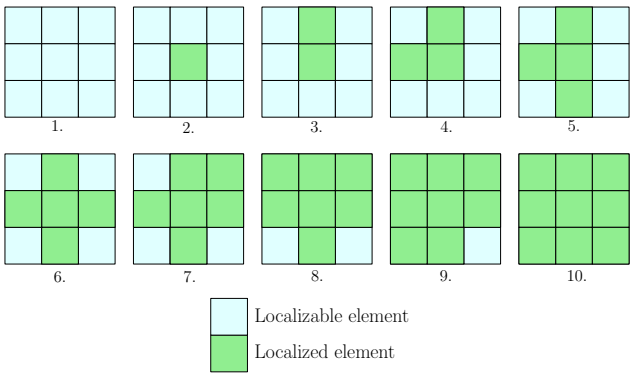

Figure 15: Illustration of the localization band spiral propagation in one time increment

3.2.3. XFEM-CZM coupling

As was mentioned in Section 2.1.2 the cohesive zone is inserted in the XFEM formulation to create a cohesive strong discontinuity (see Wolf et al. [39, 74]) :

$$\mathbf{K}\begin{Bmatrix} \mathrm{d}\alpha \\ \mathrm{d}\beta \end{Bmatrix} = \begin{Bmatrix} \mathbf{F}^{\alpha}_{ext} \\ \mathbf{F}^{\beta}_{ext} \end{Bmatrix} - \begin{Bmatrix} \mathbf{F}^{\alpha}_{int} \\ \mathbf{F}^{\beta}_{int} \end{Bmatrix} \tag{43}$$

where $d\alpha, d\beta$ represent the nodal displacement increments of the standard and additional dofs and $\mathbf{F}_{int}$ the internal forces (with the superscript denoting correspondence to standard or additional dofs), i.e.

$$\begin{aligned} \mathbf{F}^{\alpha}_{int} &= \int_{V^e} \mathbf{B}^T \boldsymbol{\sigma} dV^e \\ \mathbf{F}^{\beta}_{int} &= \int_{V^e} \mathbf{B*}^T \boldsymbol{\sigma} dV^e + \boldsymbol{F_{coh}} \end{aligned} \tag{44}$$

In this work we consider displacement control so there are no external tractions applied to the finite elements. Thus, the external forces corresponding to the standard and additional dofs $\mathbf{F}^{\alpha}_{ext}$ and $\mathbf{F}^{\beta}_{ext}$ in 43 are neglected.

The element stiffness matrix $\mathbf{K}$ in 43 reads:

$$\mathbf{K} = \begin{bmatrix} \int_{V^e} \mathbf{B}^T \mathbf{L} \mathbf{B} dV^e & \int_{V^e} \mathbf{B}^T \mathbf{L} \mathbf{B*} dV^e \\ \int_{V^e} \mathbf{B*}^T \mathbf{L} \mathbf{B} dV^e & \int_{V^e} \mathbf{B*}^T \mathbf{L} \mathbf{B*} dV^e + \int_{\Gamma_D} \mathbf{N*}^T \boldsymbol{C}_{\mathrm{loc}} \mathbf{N*} d\Gamma \end{bmatrix} \tag{45}$$

Where $\boldsymbol{C}_{\mathrm{loc}}$ is defined in 21 and $\mathbf{L}$ in 32, $\mathbf{B}$ represents the spatial derivatives matrix of the shape functions, $\mathbf{B*}$ the spatial derivatives matrix of the $(H(x) - H_j)N_j$ functions, $\mathbf{N*} = \mathbf{R}^{-1}\mathbf{N}$, with $\mathbf{R}$ the transformation matrix for the passage from the global to the local framework of the cohesive band and V^e the finite element volume and Γ_D the discontinuity surface.

The cohesive tangent matrix $\boldsymbol{C}_{\mathrm{loc}}$ is calculated only when an element is localized. At the moment of localization the band orientation is determined and the displacement jump vector $\boldsymbol{\delta}$ is calculated, Eq.14. This is done in the following sense:

$$\boldsymbol{\delta} = \mathbf{N*}\boldsymbol{U} \tag{46}$$

where $\boldsymbol{U}$ is the nodal displacements vector calculated by Abaqus. Since the displacement jump vector is non-zero, the equivalent displacement jump Δ is also non-zero.

The cohesive forces, appearing in Eq.44, are expressed as:

$$\boldsymbol{F_{coh}} = \boldsymbol{F^0_{int}} - \int_{\Gamma_D} \mathbf{N^*}^T (D\,\boldsymbol{t_0}) d\Gamma \tag{47}$$

The initial tractions $\boldsymbol{t_0}$ are calculated from the internal forces of the element in that instance via the solution of the linear system expressed by:

$$\boldsymbol{F^0_{int}} = \int_{\Gamma_D} \mathbf{N^*}^T \boldsymbol{t_0}\, d\Gamma \tag{48}$$

where $\boldsymbol{F^0_{int}}$ is the vector of the internal forces of the element at the time of localization. This vector is, thus, constant while being a priori different for each element. Indeed, $\boldsymbol{t_0}$ takes a value that depends on the element since it results from its current state at the moment of localization.

The reason why the initial tractions are not calculated directly from the stress tensor at localization onset ($\underset{\sim}{\sigma}_0$), in the sense of Eq. 12, is because this calculation creates inaccuracies that lead to convergence issues at localization onset and non-physical reaction force jumps. For the same reasons the calculation of $\boldsymbol{F_{coh}}$ is not treated as $\boldsymbol{F_{coh}} = \int_{\Gamma_D} \mathbf{N}^T((1-D)\,\boldsymbol{t_0}) d\Gamma$ but rather as expressed in Eq.47.

According to 47, the cohesive forces are consequently calculated as a damaged state correction to the predicted healthy state.

3.2.4. Integration scheme

For the integration of the XFEM element integrals associated with the stiffness matrix and force vectors the method that finds the widest use is the element subdivision [30, 31, 36]. In the 3D case the volumes created by the crack ($V^- + V^+ = V^e$) are divided into tetrahedra and standard Gauss integration is applied using the newly distributed integration points of each tetrahedron. This partitioning implies the projection of state variables from the old GPs onto the new ones, which especially in the case of path-dependence can become both

numerically demanding and might lead to inaccuracies. Other methods have appeared in the literature. One can notably cite (i) the use of a great number of GPs [75] ensuring that there will always be at least one GP on both sides of the discontinuity; which is a practical but numerically cumbersome scheme, or (ii) the the replacement of the Heaviside function by continuous enrichment functions as in Martin et al. [76], but again using a rather large number of GPs.

In the present work the integration scheme adopted is the Volume Averaging Integration (VAI) inspired by Belytschko et al. [29] approach and applied in Nikolakopoulos et al. [77]. This method alleviates the need for GPs on both sides of the discontinuity. VAI is a modified quadrature rule that uses standard Gauss points and performs the integration twice, averaging the contributions of the two sub-volumes as follows:

$$\rho = \frac{V^-}{V^e} \sum_{i=1}^{nint} f\big(-0.5, \underline{\xi_i}, ...\big) w_i J_a(\underline{\xi_i}) + \frac{V^+}{V^e} \sum_{i=1}^{nint} f\big(+0.5, \underline{\xi_i}, ...\big) w_i J_a(\underline{\xi_i}) \quad (49)$$

where ρ can be the stiffness matrix or the internal forces vector, $nint$ the number of Gauss points, $\underline{\xi_i}$ the vector containing the local coordinates of the Gauss point, w_i the weight of the Gauss point, J_a the determinant of the Jacobian and $f(\cdot)$ a function of the position of the integration point with respect to the discontinuity. According to the contribution of a given sub-volume to ρ consists in a sum over all integration points of the element while assigning the value +0.5 (V^+) or -0.5 (V^-) to H and weighting the result by the ratio of the sub-volume over the total volume of the element.

The integration scheme is completed by the use of the B-Bar approach (see Hughes [78]) in order to deal with volumetric locking. For more information on the implementation of the B-bar approach in the framework of ABAQUS the reader can refer to Shi et al. [79].

The ability of VAI to accurately calculate the displacement jump when GPs do not exist on both sides of the discontinuity is presented by means of a simple 1D problem in the Appendix B.

In Algo. 3 the Abaqus user element (UEL) algorithm is presented.

Algorithm 3: UEL algorithm

ABAQUS analysis increment k;
    UEL called for element j;
    Internal variables updated using GTN ;
    $[K_{XFEM}]$, $[F_{XFEM}]$ matrices calculated ;
    Cohesive law variables updated using coh. law;
    $[K_{coh}]$, $[F_{coh}]$ matrices calculated ;
    Update list of localizable elements;
    Assemble j element $[K]$ and $[F]$ matrices ; // $[K] = [K_{XFEM}] + [K_{coh}]$, // $[F] = -[F_{XFEM}] - [F_{coh}]$
    Loop 2 to 8 for all elements;
Assemble $[K]$ and $[F]$ matrices of the structure;
Resolve global system of equations;
End increment k;
    Propagate localization band ; // Band propagation algorithm 2

3.3. Stage of cracking - XFEM

The stage of localized damage in a ductile material is ultimately succeeded by cracking, i.e. a macro-crack appears in the wake of the meso-crack. In this work this corresponds to a complete loss of cohesion as soon as:

$$D = D_c \tag{50}$$

At this point the cohesive forces are reduced to zero, the element becomes standard XFEM and the localization band becomes a traction free crack.

3.4. Summary

In this section a ductile failure scenario was developed, postulating that a localization band can either precede or succeed void coalescence. For this reason two different criteria were applied, employing the bifurcation criterion and a phenomenological critical porosity criterion for either case respectively. In the latter case the orientation of the band is deduced from the competition

of Mode I/II mechanisms (void growth and void distortion) manifesting themselves depending on the magnitude of the local triaxiality in the finite element. Furthermore, a triaxiality transition region was introduced leading to a mode-mixicity law. A set of numerical criteria for the 3D element localization band onset, continuity and propagation has been also developed that lead to smooth band propagation and realistic crack path results.

4. Application

In this section the methodology detailed in the previous sections is applied to various boundary value problems employing the commercial finite element code ABAQUS/std. The first step is to determine the critical values of the critical stress triaxiality, as were presented in Section 3.2.1.2, so as to better reproduce the flat-to-slant localization transition. This is done by examining the stress triaxiality evolution using only the ABAQUS in-built GTN model. In a second step, by applying the methodology to a notched axisymmetric, a flat notched and a shear specimen we seek to show that the methodology is capable to fairly reproduce the ductile fracture phenomenon, whilst being mesh independent. In a third step, the influence of user defined parameters is investigated.

4.1. Numerical procedure

The unified 3D XFEM/CZM methodology described in the previous Section has been implemented as an ABAQUS user element routine (UEL). The different specimens under consideration are meshed with 3D full integration 8-node hexahedral elements, and the loading is applied under quasi static conditions with displacement control. The discretization of the boundary value problem is achieved using ABAQUS-CAE which generates an initial input file (`~.inp`). Given that Abaqus allows only 3 dofs per node for 8-node 3D elements, the dof enrichment of the model is achieved through the addition of 'enrichment' nodes done in a modified input file created via a Python script. In the same time, each element is associated with both its initial standard nodes and its new

enrichment nodes. This modified input file is submitted to ABAQUS for analysis with the UEL. The size of the element stiffness matrix and internal forces vector is equal to the standard dofs plus the enrichment dofs, i.e. the number of dofs is not growing throughout the analysis. At the beginning of the analysis all 'enrichment' dofs are inactive and are activated as soon as localization conditions are met. The stiffness matrix and internal forces vector is calculated for each element through the UEL routine and is provided to ABAQUS, that assembles the global matrices. The global problem is solved via implicit integration with ABAQUS solver. If there is convergence of the solution of the system of equations the new nodal displacements vector is acquired, if not the solver adjusts the load increment until convergence is reached.

4.2. Analysis assumptions

Throughout this work there is no pre-existing discontinuity in any specimen. Two different mesh sizes are employed, i.e. 'coarse' with element dimensions $\approx$1x1x1mm^3 and 'fine' $\approx$0.5x0.5x0.5mm^3, in the area of interest. It is reminded that the goal of this unified methodology is its application to the numerical simulation of crack initiation and propagation within large engineering structures, so the use of extremely fine meshes is not within its scope. The elastic and hardening material parameters were chosen to reproduce the response of a mild steel. The cohesive law parameters in this part of the study have been arbitrarily chosen so as to simulate a ductile like softening behaviour. As usually done when using GTN type models, see e.g. [7, 9–11, 13, 39, 80], the material has been ascribed an initial porosity, viz. 0.1%. The material and cohesive law parameters taken into consideration are gathered in Table 2.

4.3. Flat-to-slant transition

A flat-to-slant fracture transition resulting in the well-known cup-and-cone fracture is often observed in post-mortem tensile loaded round cylindrical specimens. Indeed, in these specimens cracking starts in the middle of the specimen, and propagates under the effect of normal stresses (mode I) in high triaxiality

Table 2: Parameters related to strain hardening, microporous plasticity and the cohesive law

E	ν	R_0	R_∞	k	$q_1 = q_2$	Δ_c
200GPa	0.33	400MPa	150MPa	20	1	3mm
f_0	f_c	f_N	s_N	κ_N	D_c	γ
0.001	0.03	0.04	0.05	0.3	0.5	2

regions. Then under the dominant effect of shear stresses (mode II) it propagates inclined towards the edges, see Fig. 16. A similar behaviour is displayed in flat specimens but with a slanted crack surface through the specimen's thickness [81]. The various specimen geometries considered in the following are drawn in Fig.17, with their dimensions given in Table 3.

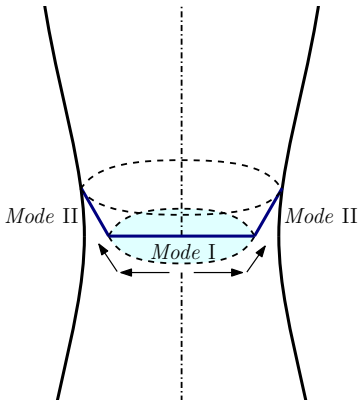

Figure 16: Cup and cone effect formation

To favour the failure in the middle of the specimen gauge length and palliate the absence of necking when using the small strain theory, specimens with large notch radii were considered, see Table 3.

4.3.1. Calibration of the critical local triaxiality values T_{sh} and T_{ten}

The calibration of the critical local triaxiality values T_{sh} and T_{ten} is needed for the void coalescence-induced localization criterion, see Section 3.2.1.2 and Fig.11. For that purpose, numerical simulations were conducted on notched

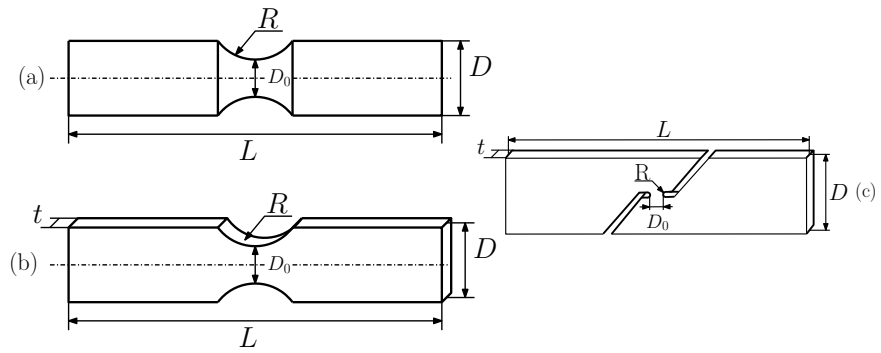

Figure 17: Specimens considered: (a) notched axisymmetric, (b) flat notched, (c) shear

Table 3: Specimen geometrical characteristics

Specimens	L(mm)	D(mm)	D_0(mm)	R(mm)	t(mm)
(a) Notched Axisym.	63	10.8	6	6.2	-
(b) Flat notched	100	18	10	10	2
(c) Shear	143	25	5	1	2

axisymmetric and flat specimens using GTN model and standard FEM, and the stress triaxiality ratio and void volume fraction were extracted in various finite elements located inside the cross section at various increments, see Fig.18. The local triaxiality T is plotted with respect to the porosity f in Fig.19

According to Fig.19 (left) related to the notched axisymmetric specimen, as expected: (i) the closer the element is to the middle the higher the local triaxiality; when moving towards the edge the triaxiality decreases. One can also observe that at $f = f_c$, the stress triaxialiy T is greater than 0.57 in the first three elements. (ii) around the 4th element there appears a change in the behaviour with T being more or less constant (slightly lower than 0.5) (iii) For the last element, lying in the region where a slanted path is expected, there is a drop in the triaxiality at the very beginning followed by a slight decrease leading to a value of $T \approx 0.25$ at $f = f_c$.

According to Fig.19 (right) related to the flat notched specimen it can be

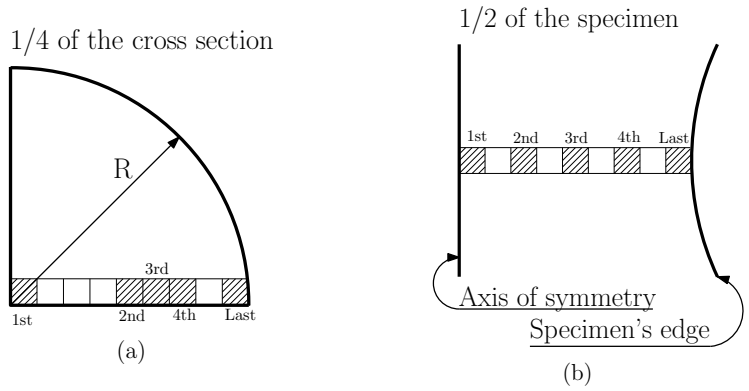

Figure 18: Elements considered: (a) Notched axisymmetric specimen - through-the-cross-section view, (b) Flat notched specimen - front view

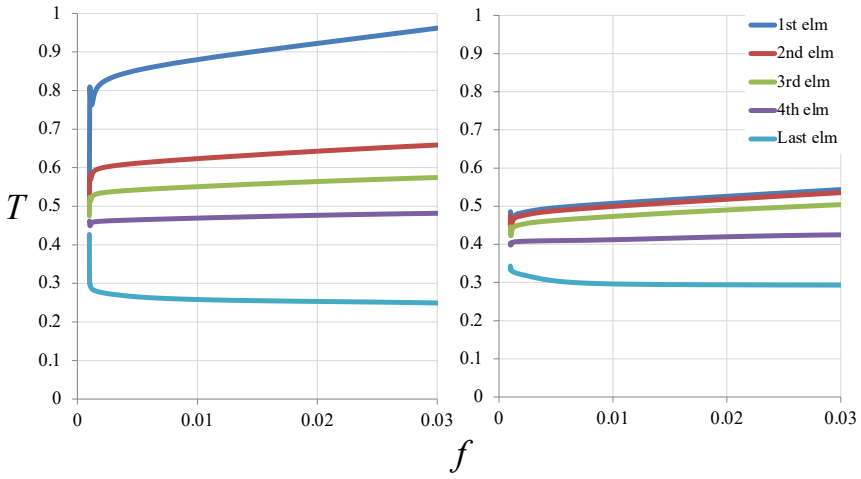

Figure 19: Evolution of triaxiality with respect to the element's porosity for five elements along the notched axisymmetric specimen's radius (left) and the flat notched specimen's width (right)

seen that the local triaxiality remains more or less constant for elements situated closer to the plane of symmetry of the specimen, with the highest value $T \approx 0.57$ and takes lower values when approaching the edge, with lowest value $T \approx 0.29$.

575 The T_{sh} and T_{ten} values should be the same for both specimens. We consider, thus, the following scenario:

1. The triaxiality transition zone (delimited by T_{sh} and T_{ten}) should lie close to the region [0.43,0.52] for a typical steel material ([70] see Section 3.2.1.2). In order for the criterion to give consistent results for both specimens, the critical local triaxiality values T_{sh} and T_{ten} should be situated approximately in this triaxiality region.

2. For the axisymmetric specimen we expect a localization: in Mode I for the centre element, then a transition (or mixed-Mode) around the 4th element and, finally, in Mode II for the last.

3. For the flat notched specimen it is expected that the band will appear more or less slanted through the thickness in all elements (mixed-Mode or Mode II). This implies that $T_{ten} = 0.57$ (the triaxiality value of the centre element for $f = f_c$).

For all subsequent analyses the values used are $T_{sh} = 0.41$ and $T_{ten} = 0.57$, both determined numerically so as to reproduce the fracture surface for both specimens.

4.4. Unified GTN-XFEM/CZM methodology results

In Figs.20 and 21 is depicted the global response in terms of reaction force vs displacement for the three specimens (in Fig.17). The proposed XFEM/CZM methodology for the two meshes (utilizing the FE developed seen in Fig.7) is compared with the in-built Abaqus GTN model (standard FEM) and the GTN model with coalescence effects or f^* method from Tvergaard and Needleman[6] (standard FEM). In the latter case the coefficients used are $f_c = 0.03$, $f_U^* = 1$ and $f_F = 0.15$ (for more explanations see equations 2.3 and 2.4 in [6]). The porosity at localization incipience f_c is chosen to be the same both for the f^* method and the XFEM/CZM method for a better comparison. According to Figs.20a and 20b, it can be seen that for the two tensile specimens the mesh size has little if no effect on the obtained results when the XFEM-CZM methodology is used. Indeed, the pathological mesh dependency of the GTN model, visible in Figs.20a and 20b when using standard FE, is overcome thanks to the use of the proposed methodology combining XFEM and CZM. Concerning

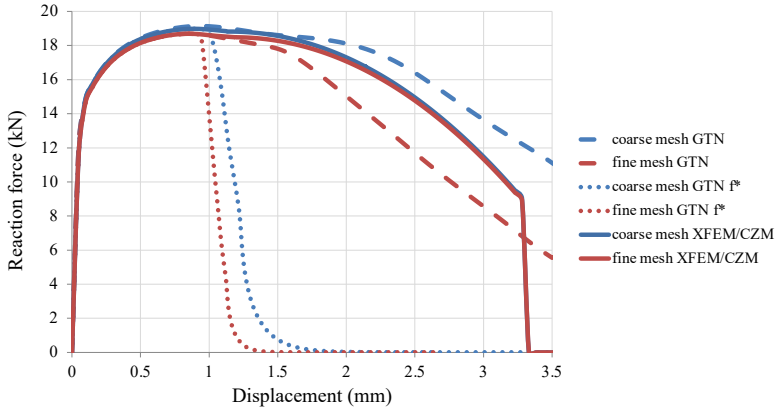

(a)

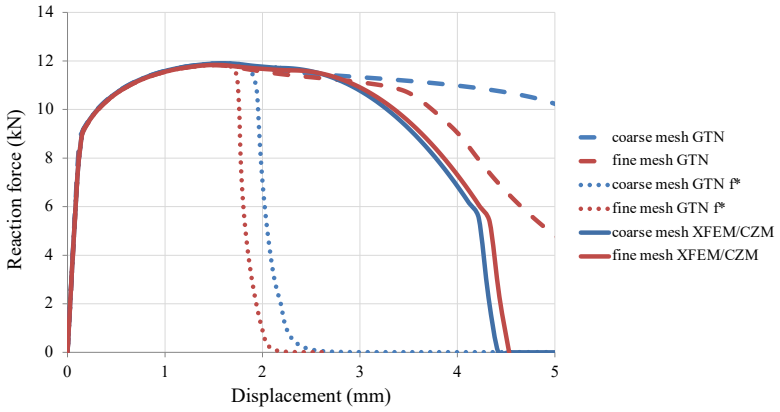

(b)

Figure 20: Mesh size dependence study: (a) Notched axisymmetric specimen, (b) Flat notched specimen - A comparison of in-built f-based Gurson model, in-built f*-based GTN model and XFEM-CZM model

the f* method, it can be seen that in this case the mesh size influence is less acute than in the case of the standard GTN, but there is a non-physical abrupt softening behavior. For the shear specimen, Fig.21, there is an influence of the mesh size in the hardening regime, that means before the localization onset and accordingly before the activation of the XFEM-CZM method, and then in the

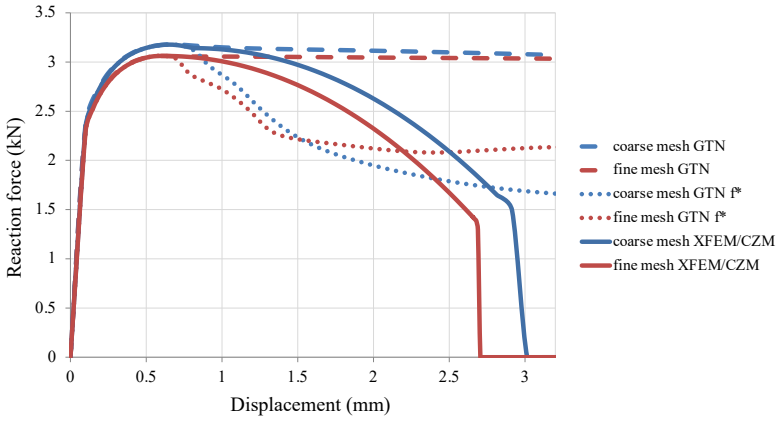

Figure 21: Mesh size dependence study: Shear specimen - A comparison of in-built f-based Gurson model, in-built f*-based GTN model and XFEM-CZM model

softening regime. This is explained by the presence of too few elements in the region of interest (only two elements on the $R1$ notch arc, viz.Fig.17). It is noteworthy that in this work void growth in pure shear is not treated, since the standard GTN model is used. Indeed, the evolution of the porosity f is due only to the void nucleation which explains the presence of the large plateau that appears in Fig.21 when only the standard FE is used (dashed lines). A better representation of the phenomenon would be obtained via the use of a modified GTN model taking into account void growth at negative and null triaxialities (e.g. [7, 9, 10]). Regarding the results obtained with the f^* method, the initial load drop is due to the fact that a few elements have attained the f_c, but since most of the elements cannot attain this porosity there is no complete loss of load carrying capacity.

The objectivity of the proposed unified methodology has been established in terms of mesh size, but another factor that could have an impact on the obtained numerical results is the mesh orientation. However, with the type of test specimens studied in this article it is difficult to study the influence of the mesh orientation. Indeed, the shape of the test specimens and the use of hexahedral elements, allows Abaqus-CAE only little flexibility in the meshing. For this

reason the influence of mesh orientation is studied here through the comparison of the numerical results obtained with the flat notched specimen using both a structured and an unstructured mesh. It can be seen in Fig.22 that quasi-similar RF vs. Displacement curves are obtained with all four meshes, which means that the mesh orientation has a negligible influence on the numerical results.

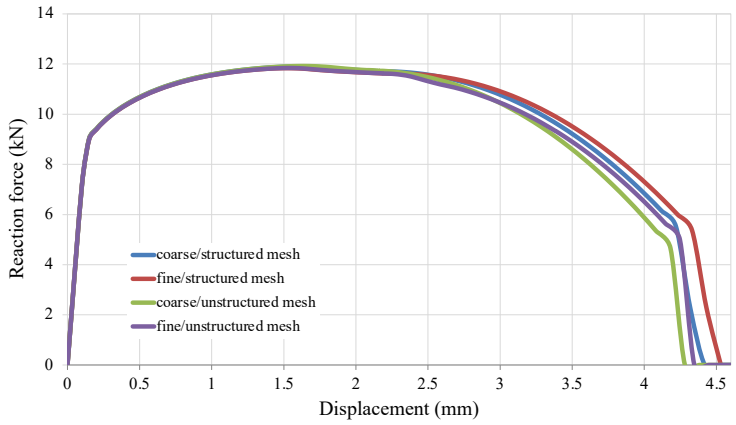

Figure 22: Mesh orientation dependence study: Flat notched specimen - RF vs Displacement response

It would be interesting here to discuss the different localization mechanisms appearing in the numerical simulations of the three specimens. In the case of the shear specimen the criterion that is satisfied first is $min[det(\underset{\sim}{Q})] < 0$ in 36, viz. plastic instability triggers the localization as expected. On the other hand in the case of the notched axisymmetric and flat notched specimens the criterion that triggers localization is the phenomenological f_c criterion in 38, viz. localization results from void coalescence.

In Fig 23 and 24 the evolution of the decohesion variable D is plotted for the three specimens under consideration (coarse mesh) in elements whose location is specified in Fig.19. Localization onset (criterion 36 or 38) and macro-crack onset (criterion 50) for each specimen are indicated by a vertical dashed line and a dotted line respectively. According to Fig.23, localisation appears earlier and propagates faster in the axisymmetric specimen than in the flat one. That

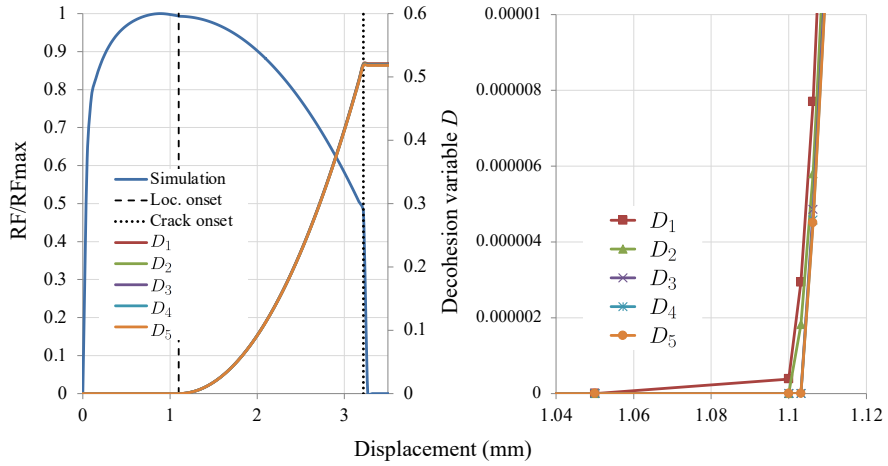

(a)

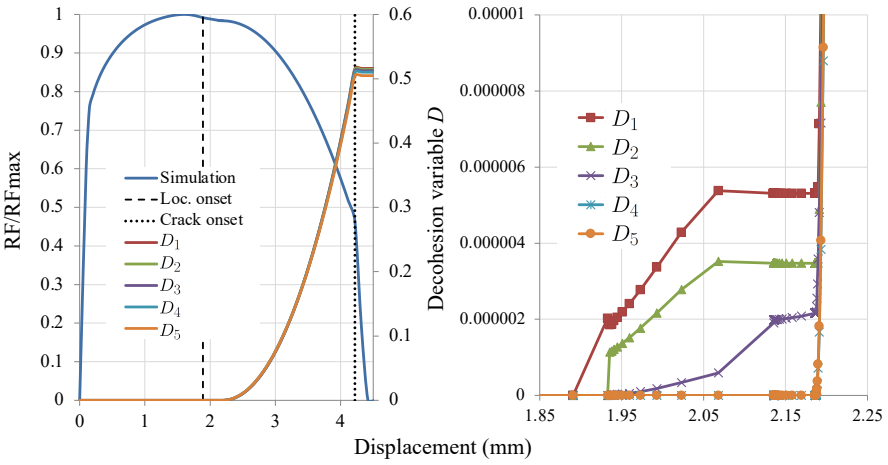

(b)

Figure 23: Notched axisymmetric (a) and Flat notched specimen (b) - RF/RF_{max} vs Displacement response and decohesion variable D vs Displacement evolution for five elements along a radius/width (left) and Decohesion variable D vs Displacement evolution for five elements along a radius/width - zoom in the region of localization initiation (right)

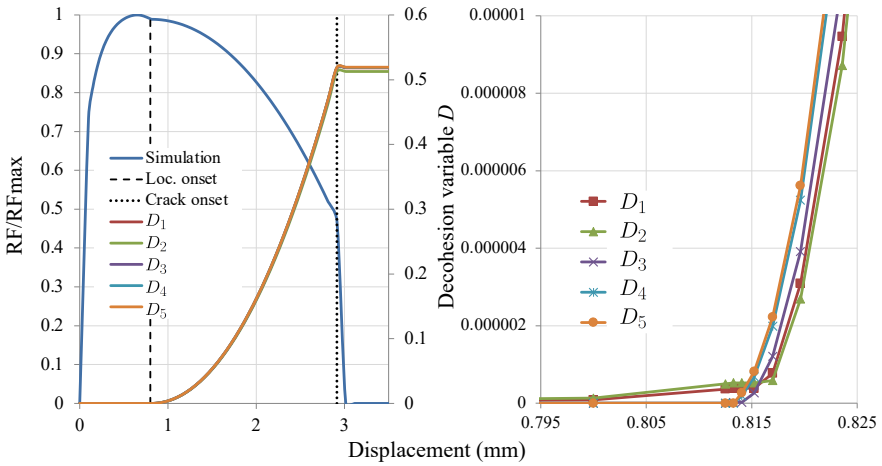

Figure 24: Shear specimen - RF/RF_{max} vs Displacement response and decohesion variable D vs Displacement evolution for five elements along the region of interest (left) and Decohesion variable D vs Displacement evolution for five elements along the region of interest - zoom in the region of localization initiation (right)

is to be expected since the triaxiality is generally higher for the axisymmetric specimen, see Fig.19, leading to a quicker attainment of f_c. According to Fig.23a (right), it can be seen that in the axisymmetric specimen the band has crossed the whole cross-section in two increments, while for the flat, Fig.23b (right), it takes a much larger number of increments. Once the band has propagated through the whole cross section, then D increases rapidly. On the other hand localization initiates and propagates fast for the shear specimen, see Fig.24, since it is triggered by the bifurcation criterion and it is, thus, independent of the evolution of porosity.

As to the crack path almost identical results are obtained with both meshes for all specimens, see Fig. 25 to 27. The expected mode I to mode II transition is well reproduced for the notched axisymmetric specimen, Fig. 28. In the case of the notched axisymmetric specimen the radius of the 'flat' region can become larger if a smaller value of T_{ten} is used. If the value of T_{ten} is very high then this radius tends to 0 and the band initiates and propagates under Mode II (or

mixed Mode I/II). According to Fig.30, for the shear specimen the band appears in the thickness of the area of interest and close, but not on, the specimen's edge (increment 1). It then reaches the free surfaces (increment 2) and propagates towards the other end (increment 3 to 5).

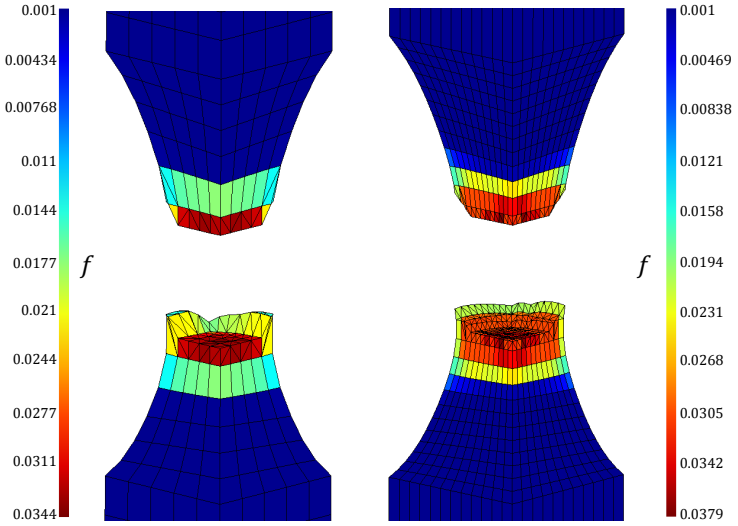

Figure 25: Crack surfaces of notched axisymmetric specimen - coarse (left) and fine (right) mesh. Porosity f distribution

An inflection is visible just after the maximum of the reaction force in Figs.23-24. This inflection can be attributed to a cocktail involving the small strain hypothesis, the nucleation law standard deviation s_N and the critical porosity f_c. The influence of the these parameters is studied in Section 4.5.

Through the application of the GTN-XFEM/CZM methodology to a notched axisymmetric, a flat notched and a shear specimen the methodology is seen to be able to fairly reproduce the crack surface and the softening regime in a mesh objective manner. In the following study the 'coarse' mesh will be used in all cases.

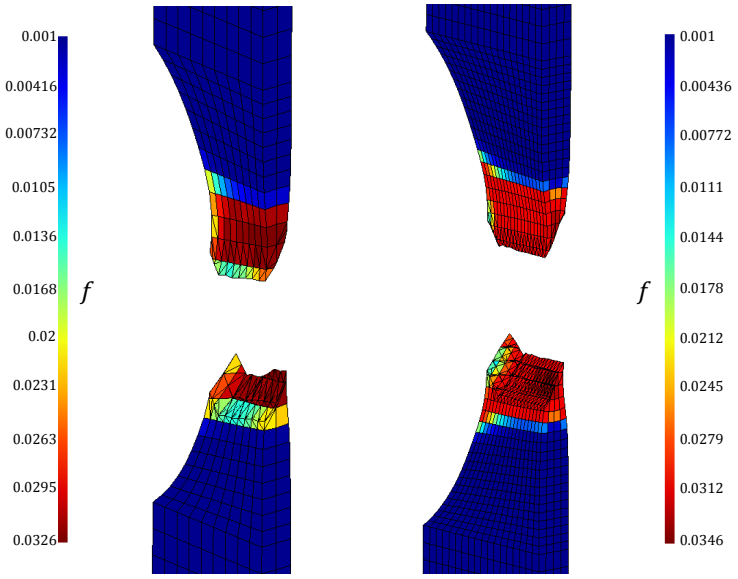

Figure 26: Crack surfaces of flat notched specimen - coarse (left) and fine (right) mesh. Porosity f distribution

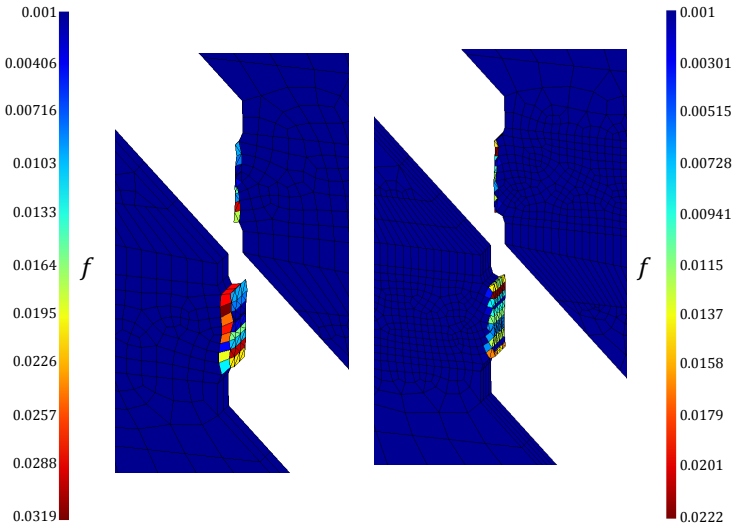

Figure 27: Crack surfaces: (a) shear specimen - coarse (left) and fine (right) mesh. Porosity f distribution

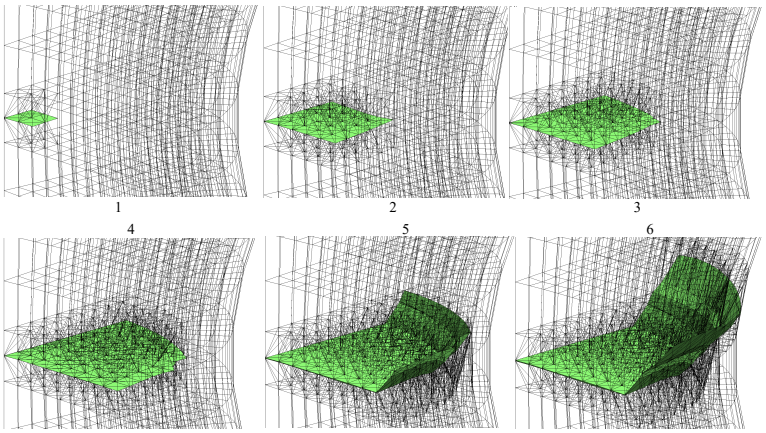

Figure 28: Band propagation in the notched axisymmetric specimen (fine mesh)

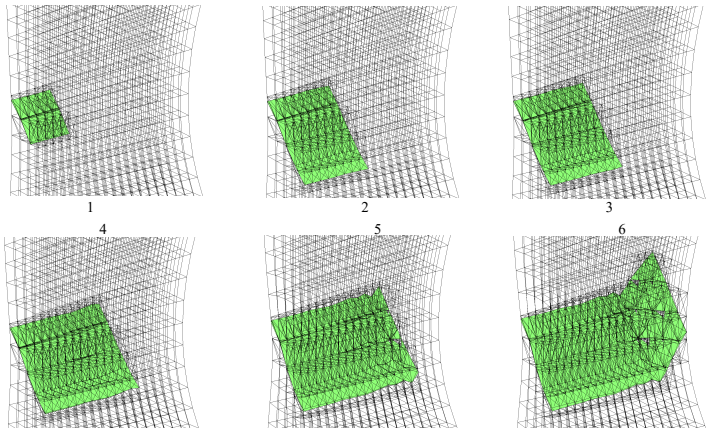

Figure 29: Band propagation in the flat notched specimen (fine mesh)

4.5. Parametric study

According to Eq.20 and 47, the softening response is controlled by the cohesive parameters Δ_c, γ and D_c, the critical porosity f_c and the nucleation law parameters - f_N, κ_N and s_N. In the following sub-sections the influence of these parameters on the global response of the notched axisymmetric specimen (coarse mesh) is discussed. Similar results are equally obtained for the flat notched and shear specimens. The parameters used are given in Table 4.

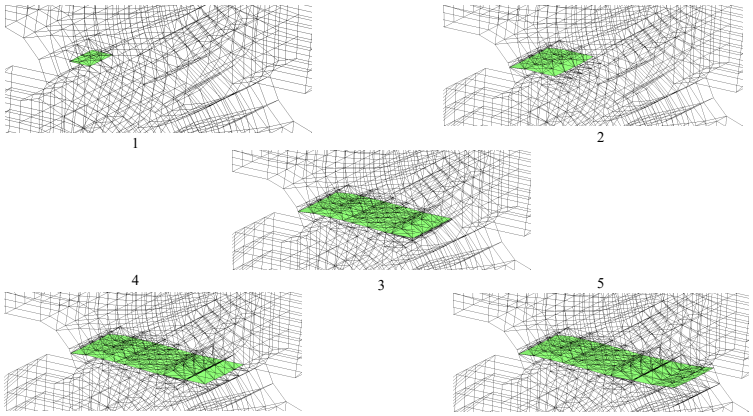

Figure 30: Band propagation in the shear specimen (fine mesh)

Table 4: Cohesive law and nucleation law parameters for parametric study

Coh. Params.	$\Delta_c(mm)$	γ	D_c		Nuc. Law	κ_N	s_N	f_N
Combinations Fig.31	2 to 4	1 to 3	0.3 to 1		1	0.3	0.05	0.04
					2		0.1	
					3		0.15	

4.5.1. Cohesive parameters

For the loading cases considered in this work the form of the CZM softening law directly influences the shape of the global response in the softening regime. Thus, different behaviours in the spectrum between brittle like and pure ductile fracture can be modelled by changing the values of the three parameters of the cohesive law in use. The results of this parametric study can be seen for different: γ values in Fig.31(a), Δ_c values in Fig. 31(b), D_c values in Fig. 31(c). According to Fig.31(a), for $\gamma = 1$ we have a linear response, that is not very physical for ductile materials, while for increasing γ the softening response curve becomes increasingly convex. According to Fig.31(b), increasing D_c leads to a more progressive degradation of the specimen resistance and further later failure. According to Fig.31(c), by reducing the critical value of the decohesion variable D_c the failure becomes more premature. In all the presented cases

the softening commences at the same increment and it is triggered by the void coalescence-induced localization criterion (involving f_c).

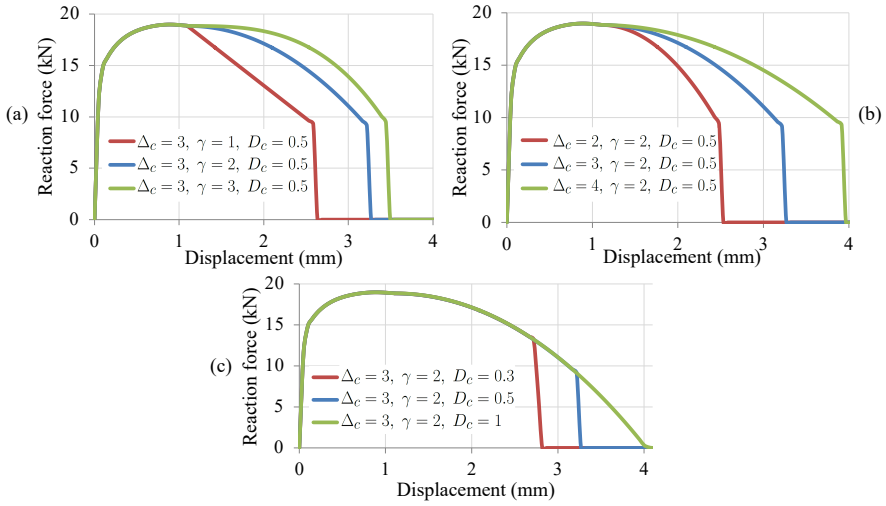

Figure 31: Notched axisymmetric specimen - RF vs Displacement response for different cohesive laws

4.5.2. Nucleation law

As previously mentioned, the apparent inflection discussed in Section 4.4 is notably influenced by the void nucleation law parameters in Eq.11. In Fig. 32 three different laws centered in $\kappa_N = 0.3$ but with different standard deviations s_N are used: a small standard deviation yields a narrow bell-shape kinetics law whereas a large standard deviation yields a wide bell-shape kinetics law. In Fig. 33 (left) the response of the notched axisymmetric specimen using the ABAQUS in-built GTN model for the three laws is plotted. For the first nucleation law, characterized by a small standard deviation, there is an inflection whereas for the third nucleation law, characterized by a large standard deviation, this inflection vanishes. This phenomenon is more clearly seen if we zoom on the said region of the reaction force-displacement curve, see Fig. 33 (right). However, at the same time, using a larger s_N value we are lead to a non-zero porosity nucleation rate for zero plastic strain, which is not entirely physical. On the other hand

the nucleation law also influences the softening regime since the three variables κ_N, s_N and f_N determines the time at which f_c will be attained, thus, the time of localization onset. Consequently, the XFEM-CZM method is not responsible for the deflection.

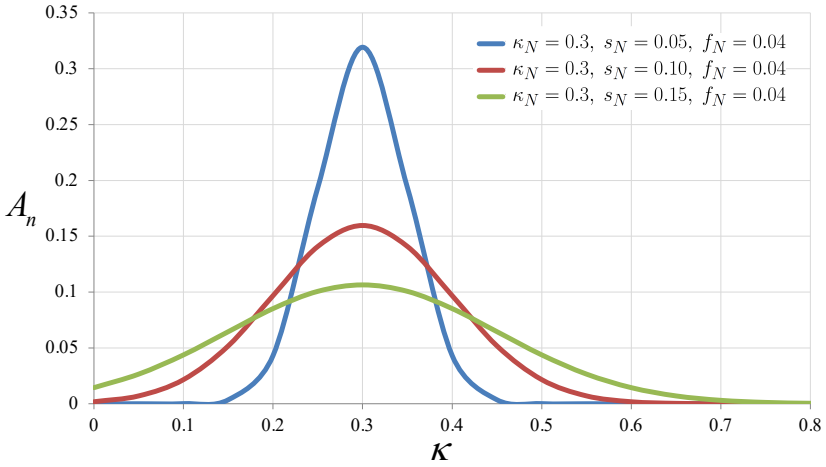

Figure 32: Normal distribution of the nucleation law Eq.11 for different nucleation law parameters

4.5.3. Critical porosity

As expected the critical porosity f_c in Eq.38, that triggers the void coalescence induced localization, influences the overall response, see Fig. 34, as the higher its value the more localization is delayed. This delay in the introduction of the softening regime can be clearly seen in the zoomed-in localization region in Fig.34 (right). In general a smoother transition from diffuse damage to localization, in terms of RF vs displacement can be achieved using a larger s_N and a smaller f_c value.

5. Concluding remarks

This work addresses the problem of the numerical treatment of ductile fracture in metallic structural materials. The three successive stages of void nucle-

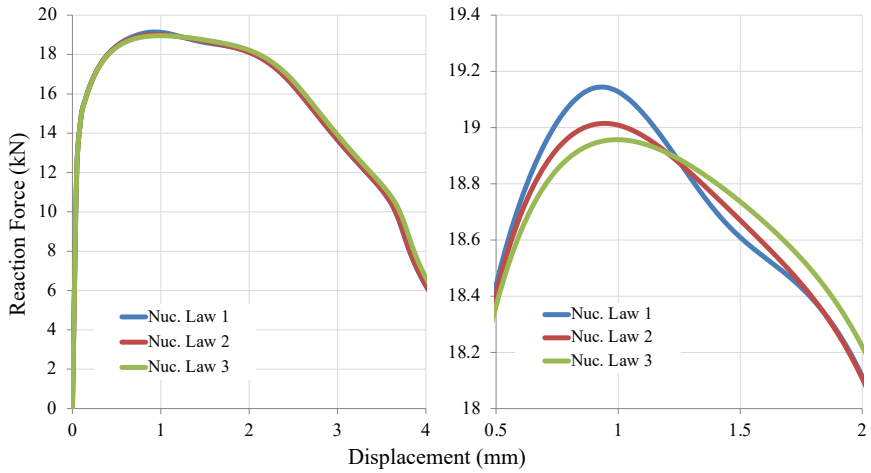

Figure 33: Notched axisymmetric specimen - RF vs Displacement response for different nucleation laws (left) and Zoom-in the region of apparent inflection (right)

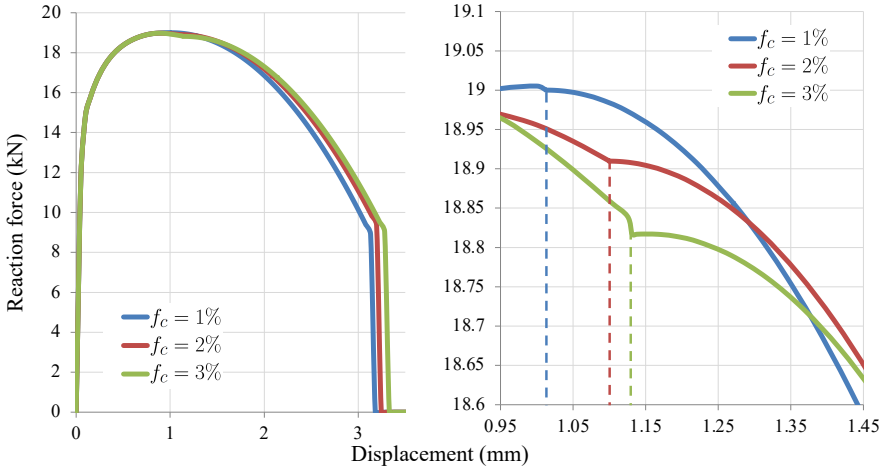

Figure 34: Notched axisymmetric specimen - RF vs Displacement response for different critical porosities f_c (left) and Zoom-in the region of apparent inflection (right)

ation and growth, localization and crack opening are reproduced in a unified three-dimensional methodology that combines the GTN model for the description of diffuse damage in the context of standard FEM, the eXtended FEM for

kinematic representation of the traction free crack and a coupling of the XFEM with the CZM for the treatment of the damage intermediate localization phase and the induced degradation of the mechanical properties of the material. Particular interest is given to the criteria for the passage from the diffuse damage to the localization stage and the determination of the orientation of the localization plane. The localization scenario consists of two cases, either preceding or succeeding void coalescence. Accordingly, two numerical cases are considered; in the first case the bifurcation analysis is applied while in the latter a porosity triggered criterion is adopted, that accounts for the competition between the Mode I/II localization mechanisms at play. This way the flat-to-slant transition is fairly reproduced numerically; namely the 'cup and cone' effect. Some operational localization onset and propagation criteria are proposed. Additionally, a flexible cohesive 'power' law is developed and the volume averaging integration scheme (VAI) is employed. The methodology is implemented as an ABAQUS user-element and applied to 3D tensile and shear specimens under quasi-static loading conditions. The unified three-dimensional methodology is shown to be able to reproduce numerically the global response, in a mesh independent manner, and lead to realistic fracture surfaces in notched axisymmetric, flat notched and shear specimens. A parametric study for the effect of user defined parameters of the cohesive and void nucleation laws is realized, showing that the method can indeed reproduce a wide variety of softening responses. It can be concluded that the proposed methodology successfully simulates the complex phenomenon of ductile fracture in three dimensions. Since ductile fracture is a phenomenon that can involve important geometrical changes, the incorporation of the large strain theory would be a useful advance to the current method, a work in progress, as well as the treatment of multiple crack initiation sites, rarely addressed in the literature.

Acknowledgement

The authors would like to acknowledge the French Direction Générale de l'Armement (DGA) for its support.

Declaration of Competing Interests

None

References

[1] L. M. Kachanov, Time of the rupture process under creep conditions, Isv. Akad. Nauk. SSR. Otd. Tekh. Nauk. (1958) 26–12.

[2] J. Lemaitre, A Continuous Damage Mechanics Model for Ductile Fracture, Journal of Engineering Materials and Technology 107 (1) (1985) 83–89. doi:10.1115/1.3225775.

[3] P. Perzyna, Stability of flow processes for dissipative solids with internal imperfections, ZAMP Zeitschrift für angewandte Mathematik und Physik 35 (6) (1984) 848–867. doi:10.1007/BF00945448.

[4] G. Rousselier, Ductile fracture models and their potential in local approach of fracture, Nuclear Engineering and Design 105 (1) (1987) 97–111. doi:10.1016/0029-5493(87)90234-2.

[5] A. L. Gurson, Continuum theory of ductile rupture by void nucleation and growth, Journal of Engineering Materials and Technology 99 (76) (1977) 2–15.

[6] V. Tvergaard, A. Needleman, Analysis of the cup-cone fracture in a round tensile bar, Acta Metallurgica 32 (1) (1984) 157–169. doi:10.1016/0001-6160(84)90213-X.

[7] P. Longère, A.-G. Geffroy, B. Leblé, A. Dragon, Modeling the Transition between Dense Metal and Damaged (Microporous) Metal Viscoplasticity, International Journal of Damage Mechanics 21 (7) (2012) 1020–1063. doi:10.1177/1056789511427472.

[8] P. Longère, A. Dragon, Description of shear failure in ductile metals via back stress concept linked to damage-microporosity softening, Engineering Fracture Mechanics 98 (2013) 92–108. doi:10.1016/j.engfracmech.2012.11.009.

[9] K. Nahshon, J. Hutchinson, Modification of the Gurson Model for shear failure, European Journal of Mechanics - A/Solids 27 (1) (2008) 1–17. doi:10.1016/j.euromechsol.2007.08.002.

[10] K. Nahshon, Z. Xue, A modified Gurson model and its application to punch-out experiments, Engineering Fracture Mechanics 76 (8) (2009) 997–1009. doi:10.1016/j.engfracmech.2009.01.003.

[11] Y. Shinohara, Y. Madi, J. Besson, Anisotropic ductile failure of a high-strength line pipe steel, International Journal of Fracture 197 (2) (2016) 127–145. doi:10.1007/s10704-015-0054-x.

[12] A. A. Benzerga, J. Besson, Plastic potentials for anisotropic porous solids, European Journal of Mechanics, A/Solids 20 (3) (2001) 397–434. doi:10.1016/S0997-7538(01)01147-0.

[13] A. A. Benzerga, J. Besson, A. Pineau, Anisotropic ductile fracture: Part II: Theory, Acta Materialia 52 (15) (2004) 4639–4650. doi:10.1016/j.actamat.2004.06.019.

[14] M. Gologanu, J. B. Leblond, J. Devaux, Approximate models for ductile metals containing non-spherical voids-Case of axisymmetric prolate ellipsoidal cavities, Journal of the Mechanics and Physics of Solids 41 (11) (1993) 1723–1754. doi:10.1016/0022-5096(93)90029-F.

[15] M. Gologanu, J.-b. Leblond, J. Devaux, Approximate Models for Ductile Metals Containing Nonspherical Voids—Case of Axisymmetric Oblate Ellipsoidal Cavities, Journal of Engineering Materials and Technology 116 (3) (1994) 290–297. doi:10.1115/1.2904290.

[16] M. R. Seabra, P. Šuštarič, J. M. Cesar De Sa, T. Rodič, Damage driven crack initiation and propagation in ductile metals using XFEM, Computational Mechanics 52 (1) (2013) 161–179. doi:10.1007/s00466-012-0804-9.

[17] Z. P. Bažant, G. Pijaudier-Cabot, Nonlocal Continuum Damage, Localization Instability and Convergence, Journal of Applied Mechanics 55 (2) (1988) 287–293. doi:10.1115/1.3173674.

[18] M. Shakoor, V. M. Trejo Navas, D. Pino Munõz, M. Bernacki, P.-O. Bouchard, Computational Methods for Ductile Fracture Modeling at the Microscale, Archives of Computational Methods in Engineering 26 (4) (2019) 1153–1192. doi:10.1007/s11831-018-9276-1.

[19] P. Longère, A. G. Geffroy-Grèze, B. Leblé, A. Dragon, Ship structure steel plate failure under near-field air-blast loading: Numerical simulations vs experiment, International Journal of Impact Engineering 62 (2013) 88–98. doi:10.1016/j.ijimpeng.2013.06.009.

[20] J. Wulf, T. Steinkopff, H. F. Fischmeister, FE-simulation of crack paths in the real microstructure of an Al(6061)/SiC composite, Acta Materialia 44 (5) (1996) 1765–1779. doi:10.1016/1359-6454(95)00328-2.

[21] P. E. McHugh, P. J. Connolly, Micromechanical modelling of ductile crack growth in the binder phase of WC-Co, Computational Materials Science 27 (4) (2003) 423–436. doi:10.1016/S0927-0256(03)00045-4.

[22] J. Mediavilla, R. H. Peerlings, M. G. Geers, A robust and consistent remeshing-transfer operator for ductile fracture simulations, Computers

and Structures 84 (8-9) (2006) 604–623. doi:10.1016/j.compstruc.2005.10.007.

[23] S. Feld-Payet, V. Chiaruttini, J. Besson, F. Feyel, A new marching ridges algorithm for crack path tracking in regularized media, International Journal of Solids and Structures 71 (2015) 57–69. doi:10.1016/j.ijsolstr.2015.04.043.

[24] M. Shakoor, P.-O. Bouchard, M. Bernacki, An adaptive level-set method with enhanced volume conservation for simulations in multiphase domains, International Journal for Numerical Methods in Engineering 109 (4) (2017) 555–576. doi:10.1002/nme.5297.

[25] H. Borouchaki, P. Laug, A. Cherouat, K. Saanouni, Adaptive remeshing in large plastic strain with damage, International Journal for Numerical Methods in Engineering 63 (1) (2005) 1–36. doi:10.1002/nme.1274.

[26] P. Areias, J. Reinoso, P. Camanho, T. Rabczuk, A constitutive-based element-by-element crack propagation algorithm with local mesh refinement, Computational Mechanics 56 (2) (2015) 291–315. doi:10.1007/s00466-015-1172-z.

[27] V. Chiaruttini, D. Geoffroy, V. Riolo, M. Bonnet, An adaptive algorithm for cohesive zone model and arbitrary crack propagation, European Journal of Computational Mechanics 21 (3-6) (2012) 208–218. doi:10.1080/17797179.2012.744544.

[28] M. Ortiz, Y. Leroy, A. Needleman, A finite element method for localized failure analysis, Computer Methods in Applied Mechanics and Engineering 61 (2) (1987) 189–214. doi:10.1016/0045-7825(87)90004-1.

[29] T. Belytschko, J. Fish, B. E. Engelmann, A finite element with embedded localization zones, Computer Methods in Applied Mechanics and Engineering 70 (1) (1988) 59–89. doi:10.1016/0045-7825(88)90180-6.

[30] N. Moës, J. Dolbow, T. Belytschko, A finite element method for crack growth without remeshing, International Journal for Numerical Methods in Engineering 46 (1) (1999) 131–150. doi:10.1002/(SICI)1097-0207(19990910)46:1<131::AID-NME726>3.0.CO;2-J.

[31] S. Mariani, U. Perego, Extended finite element method for quasi-brittle fracture, International Journal for Numerical Methods in Engineering 58 (1) (2003) 103–126. doi:10.1002/nme.761.

[32] É. Budyn, G. Zi, N. Moës, T. Belytschko, A method for multiple crack growth in brittle materials without remeshing, International Journal for Numerical Methods in Engineering 61 (10) (2004) 1741–1770. doi:10.1002/nme.1130.

[33] C. Comi, S. Mariani, Extended finite element simulation of quasi-brittle fracture in functionally graded materials, Computer Methods in Applied Mechanics and Engineering 196 (41-44) (2007) 4013–4026. doi:10.1016/j.cma.2007.02.014.

[34] R. Pourmodheji, M. Mashayekhi, Improvement of the extended finite element method for ductile crack growth, Materials Science and Engineering A 551 (2012) 255–271. doi:10.1016/j.msea.2012.05.014.

[35] J. P. Crété, P. Longère, J. M. Cadou, Numerical modelling of crack propagation in ductile materials combining the GTN model and X-FEM, Computer Methods in Applied Mechanics and Engineering 275 (2014) 204–233. doi:10.1016/j.cma.2014.03.007.

[36] G. N. Wells, L. J. Sluys, A new method for modelling cohesive cracks using finite elements, International Journal for Numerical Methods in Engineering 50 (12) (2001) 2667–2682. doi:10.1002/nme.143.

[37] J. J. Remmers, R. De Borst, A. Needleman, A cohesive segments method for the simulation of crack growth, Computational Mechanics 31 (1-2 SPEC.) (2003) 69–77. doi:10.1007/s00466-002-0394-z.

[38] A. Combescure, M. Coret, T. Elguedj, F. Cazes, D. Haboussa, Cohesive laws X-FEM association for simulation of damage fracture transition and tensile shear switch in dynamic crack propagation, Procedia IUTAM 3 (2012) 274–291. doi:10.1016/j.piutam.2012.03.017.

[39] J. Wolf, P. Longère, J. M. Cadou, J. P. Crété, Numerical modeling of strain localization in engineering ductile materials combining cohesive models and X-FEM, International Journal of Mechanics and Materials in Design 14 (2) (2018) 177–193. doi:10.1007/s10999-017-9370-9.

[40] E. Mikaeili, P. Liu, Numerical modeling of shear band propagation in porous plastic dilatant materials by XFEM, Theoretical and Applied Fracture Mechanics 95 (May 2017) (2018) 164–176. doi:10.1016/j.tafmec.2018.02.018.

[41] S. Kumar, I. V. Singh, B. K. Mishra, K. Sharma, I. A. Khan, A homogenized multigrid XFEM to predict the crack growth behavior of ductile material in the presence of microstructural defects, Engineering Fracture Mechanics 205 (2019) 577–602. doi:10.1016/j.engfracmech.2016.03.051.

[42] P. Broumand, A. R. Khoei, The extended finite element method for large deformation ductile fracture problems with a non-local damage-plasticity model, Engineering Fracture Mechanics 112-113 (2013) 97–125. doi:10.1016/j.engfracmech.2013.10.002.

[43] G. Legrain, N. Moës, E. Verron, Stress analysis around crack tips in finite strain problems using the eXtended finite element method, International Journal for Numerical Methods in Engineering 63 (2) (2005) 290–314. doi:10.1002/nme.1291.

[44] C. C. Chu, A. Needleman, Void nucleation effects in biaxially stretched sheets, Journal of Engineering Materials and Technology, Transactions of the ASME 102 (3) (1980) 249–256. doi:10.1115/1.3224807.

[45] D. S. Dugdale, Yielding of steel, J. Mech. Phys. Solids 8 (1960) 100–104.

[46] G. I. Barenblatt, The formation of equilibrium cracks during brittle fracture. General ideas and hypotheses. Axially-symmetric cracks, Journal of Applied Mathematics and Mechanics 23 (3) (1959) 622–636. doi:10.1016/0021-8928(59)90157-1.

[47] G. I. Barenblatt, The Mathematical Theory of Equilibrium Cracks in Brittle Fracture, Advances in Applied Mechanics 7 (C) (1962) 55–129. doi:10.1016/S0065-2156(08)70121-2.

[48] A. Hillerborg, M. Modéer, P.-E. Petersson, Analysis of crack formation and crack growth in concrete by means of fracture mechanics and finite elements, Cement and Concrete Research 6 (6) (1976) 773–781. doi:10.1016/0008-8846(76)90007-7.

[49] A. Turon, P. P. Camanho, J. Costa, C. G. Dávila, A damage model for the simulation of delamination in advanced composites under variable-mode loading, Mechanics of Materials 38 (11) (2006) 1072–1089. doi:10.1016/j.mechmat.2005.10.003.

[50] M. Elices, G. Guinea, J. Gomez, The cohesive zone model: advantages, limitations and challenges, Engineering fracture mechanics 69 (2) (2002) 137–163. doi:10.1016/S0013-7944(01)00083-2.

[51] M. Vocialta, N. Richart, J.-F. Molinari, 3D dynamic fragmentation with parallel dynamic insertion of cohesive elements, International Journal for Numerical Methods in Engineering 109 (12) (2017) 1655–1678. doi:10.1002/nme.5339.

[52] M. Ortiz, A. Pandolfi, Finite-deformation irreversible cohesive elements for three-dimensional crack-propagation analysis, International Journal for Numerical Methods in Engineering 44 (9) (1999) 1267–1282. doi:10.1002/(SICI)1097-0207(19990330)44:9<1267::AID-NME486>3.0.CO;2-7.

[53] E. Lorentz, J. Besson, V. Cano, Numerical simulation of ductile fracture with the Rousselier constitutive law, Computer Methods in Applied Me-

chanics and Engineering 197 (21-24) (2008) 1965–1982. doi:10.1016/j.cma.2007.12.015.

[54] G. Alfano, On the influence of the shape of the interface law on the application of cohesive-zone models, Composites Science and Technology 66 (6) (2006) 723–730. doi:10.1016/j.compscitech.2004.12.024.

[55] G. Zi, T. Belytschko, New crack-tip elements for XFEM and applications to cohesive cracks, International Journal for Numerical Methods in Engineering 57 (15) (2003) 2221–2240. doi:10.1002/nme.849.

[56] N. Aravas, On the numerical integration of a class of pressure-dependent plasticity models, International Journal for Numerical Methods in Engineering 24 (7) (1987) 1395–1416. doi:10.1002/nme.1620240713.

[57] A. Pineau, A. A. Benzerga, T. Pardoen, Failure of metals I: Brittle and ductile fracture, Acta Materialia 107 (2016) 424–483. doi:10.1016/j.actamat.2015.12.034.

[58] G. Diouta Ngamy, PhD thesis (1995) - Analyse numerique de la localisation dans les materiaux rocheux, Universite des Sciences et Technologies de Lille.

[59] D. C. Drucker, Some implications of work hardening and ideal plasticity, Quarterly of Applied Mathematics 7 (4) (1950) 411–418. doi:10.1090/qam/34210.

[60] A. S. Al-Sabah, D. F. Laefer, Use of negative stiffness in failure analysis of concrete beams, Engineering Structures 126 (2016) 187–199. doi:10.1016/j.engstruct.2016.07.025.

[61] J. Besson, D. Steglich, W. Brocks, Modeling of crack growth in round bars and plane strain specimens, International Journal of Solids and Structures 38 (46-47) (2001) 8259–8284. doi:10.1016/S0020-7683(01)00167-6.

[62] T. Pardoen, J. W. Hutchinson, An extended model for void growth and coalescence, Journal of the Mechanics and Physics of Solids 48 (12) (2000) 2467–2512. doi:10.1016/S0022-5096(00)00019-3.

[63] T. Pardoen, J. Hutchinson, Micromechanics-based model for trends in toughness of ductile metals, Acta Materialia 51 (1) (2003) 133–148. doi:10.1016/S1359-6454(02)00386-5.

[64] J. Besson, Damage of ductile materials deforming under multiple plastic or viscoplastic mechanisms, International Journal of Plasticity 25 (11) (2009) 2204–2221. doi:10.1016/j.ijplas.2009.03.001.

[65] Z. L. Zhang, C. Thaulow, J. Ødegård, Complete Gurson model approach for ductile fracture, Engineering Fracture Mechanics 67 (2) (2000) 155–168. doi:10.1016/S0013-7944(00)00055-2.

[66] M. A. Sutton, W. Zhao, M. L. Boone, A. P. Reynolds, D. S. Dawicke, Prediction of crack growth direction for mode I/II loading using small-scale yielding and void initiation/growth concepts, International Journal of Fracture 83 (3) (1997) 275–290. doi:10.1023/A:1007339625267.

[67] S. Liu, Y. J. Chao, X. Zhu, Tensile-shear transition in mixed mode I/III fracture, International Journal of Solids and Structures 41 (22-23) (2004) 6147–6172. doi:10.1016/j.ijsolstr.2004.04.044.

[68] D. Haboussa, T. Elguedj, B. Leblé, A. Combescure, Simulation of the shear-tensile mode transition on dynamic crack propagations, International Journal of Fracture 178 (1-2) (2012) 195–213. doi:10.1007/s10704-012-9729-8.

[69] R. Kiran, K. Khandelwal, A triaxiality and Lode parameter dependent ductile fracture criterion, Engineering Fracture Mechanics 128 (C) (2014) 121–138. doi:10.1016/j.engfracmech.2014.07.010.

[70] Z. G. Liu, W. H. Wong, T. F. Guo, Void behaviors from low to high triaxialities: Transition from void collapse to void coalescence, International Journal of Plasticity 84 (2016) 183–202. doi:10.1016/j.ijplas.2016.05.008.

[71] Y. Bao, T. Wierzbicki, On fracture locus in the equivalent strain and stress triaxiality space, International Journal of Mechanical Sciences 46 (1) (2004) 81–98. doi:10.1016/j.ijmecsci.2004.02.006.

[72] T. Elguedj, Y. Jan, A. Combescure, B. Leblé, G. Barras, X-FEM Analysis of dynamic crack growth under transient loading in thick shells, International Journal of Impact Engineering 122 (August) (2018) 228–250. doi:10.1016/j.ijimpeng.2018.08.013.

[73] H. Hooputra, H. Gese, H. Dell, H. Werner, A comprehensive failure model for crashworthiness simulation of aluminium extrusions, International Journal of Crashworthiness 9 (5) (2004) 449–464. doi:10.1533/ijcr.2004.0289.

[74] J. Wolf, P. Longère, J. P. Crété, J. M. Cadou, Strain localization in ductile materials: Assessment of three X-FEM-based enrichment methods, Mechanics Research Communications 99 (2019) 1–7. doi:10.1016/j.mechrescom.2019.05.010.

[75] T. Elguedj, A. Gravouil, A. Combescure, Appropriate extended functions for X-FEM simulation of plastic fracture mechanics, Computer Methods in Applied Mechanics and Engineering 195 (7-8) (2006) 501–515. doi:10.1016/j.cma.2005.02.007.

[76] A. Martin, J. B. Esnault, P. Massin, About the use of standard integration schemes for X-FEM in solid mechanics plasticity, Computer Methods in Applied Mechanics and Engineering 283 (2015) 551–572. doi:10.1016/j.cma.2014.09.028.

[77] K. Nikolakopoulos, J.-P. Crété, P. Longère, Volume averaging based integration method in the context of XFEM-cohesive zone model coupling, Mechanics Research Communications 104 (2020) 103485. doi:10.1016/j.mechrescom.2020.103485.

[78] T. J. R. Hughes, Generalization of selective integration procedures to anisotropic and nonlinear media, International Journal for Numerical Methods in Engineering 15 (9) (1980) 1413–1418. doi:10.1002/nme.1620150914.

[79] J. Shi, D. Chopp, J. Lua, N. Sukumar, T. Belytschko, Abaqus implementation of extended finite element method using a level set representation for three-dimensional fatigue crack growth and life predictions, Engineering Fracture Mechanics 77 (14) (2010) 2840–2863. doi:10.1016/j.engfracmech.2010.06.009.

[80] V. Tvergaard, On localization in ductile materials containing spherical voids, International Journal of Fracture 18 (4) (1982) 237–252. doi:10.1007/BF00015686.

[81] A.-G. Geffroy, PhD Thesis (2010) - Modélisation numérique de la rupture de structures navales sous l'effet d'explosions au contact, Université de Bretagne-Sud.

Appendix A. Linearization modulus A_{ij}, B_i and G_i components calculation

Differentiating the potential Φ with respect to the internal variables:

$$\dot{\Phi} = \frac{\partial \Phi}{\partial \underset{\sim}{\sigma}} : \partial \underset{\sim}{\sigma} + \frac{\partial \Phi}{\partial \sigma_y} \frac{\partial \sigma_y}{\partial \kappa} \partial \kappa + \frac{\partial \Phi}{\partial f} \partial f = \frac{\partial \Phi}{\partial \underset{\sim}{\sigma}} : \partial \underset{\sim}{\sigma} + \frac{\partial \Phi}{\partial \sigma_y} \eta \, \partial \kappa + \frac{\partial \Phi}{\partial f} \partial f \tag{A.1}$$

Decomposing the term $\partial \Phi / \partial \underset{\sim}{\sigma}$ to a deviatoric contribution and a volumetric contribution we then have:

$$\frac{\partial \Phi}{\partial \underset{\sim}{\sigma}} = \frac{\partial \Phi}{\partial \sigma_{eq}} \underset{\sim}{n} - \frac{\partial \Phi}{\partial p_m} \frac{1}{3} \underset{\sim}{I} \tag{A.2}$$

The total porosity increment (see Eq.10) is given as:

$$\partial f = (1 - f) \partial \Delta \epsilon_v + A_n \partial \kappa \tag{A.3}$$

Considering Eq.9 :

$$\partial\kappa = \frac{1}{(1-f)\sigma_y}\left[\sigma_{eq}\partial\Delta\epsilon_d - p_m\partial\Delta\epsilon_v + \left(\Delta\epsilon_d \underset{\sim}{n} - \frac{1}{3}\Delta\epsilon_v \underset{\sim}{I}\right) : \partial\underset{\sim}{\sigma}\right] \tag{A.4}$$

and Eq.23(a) :

$$\begin{aligned}
&\partial\Delta\epsilon_d\left\{\frac{\partial\Phi}{\partial\sigma_y}\frac{\eta}{(1-f)\sigma_y}\sigma_{eq} + \frac{\partial\Phi}{\partial f}A_n\frac{1}{(1-f)\sigma_y}\sigma_{eq}\right\} + \\
&\partial\Delta\epsilon_v\left\{\frac{\partial\Phi}{\partial\sigma_y}\frac{\eta}{(1-f)\sigma_y}(-p_m) + \frac{\partial\Phi}{\partial f}\left[A_n\frac{1}{(1-f)\sigma_y}(-p_m) + (1-f)\right]\right\} + \\
&\partial\underset{\sim}{\sigma} : \left\{\frac{\partial\Phi}{\partial\sigma_y} + \left[\frac{\partial\Phi}{\partial\sigma_y}\eta + \frac{\partial\Phi}{\partial f}A_n\right]\frac{1}{(1-f)\sigma_y}\left[\Delta\epsilon_d \underset{\sim}{n} - \frac{1}{3}\Delta\epsilon_v \underset{\sim}{I}\right]\right\} = 0
\end{aligned} \tag{A.5}$$

Hence, the components A_{ij}, B_i and G_i involved in the calculation of the linearization modulus are calculated as (see Eq.27 and 30):

$$A_{11} = -\left\{\frac{\partial\Phi}{\partial p_m} + \frac{\sigma_{eq}}{(1-f)\sigma_y}\left[\left(\frac{\partial^2\Phi}{\partial\sigma_y\partial p_m}\eta + \frac{\partial^2\Phi}{\partial f\partial p_m}A_n\right)\Delta\epsilon_d + \Delta\epsilon_v\eta\frac{\partial^2\Phi}{\partial\sigma_y\partial\sigma_{eq}}\right]\right\} \tag{A.6}$$

$$\begin{aligned}
A_{12} = -\Bigg\{&\frac{\partial\Phi}{\partial\sigma_{eq}} + \frac{\eta}{(1-f)\sigma_y}(-p_m)\left(\Delta\epsilon_d\frac{\partial^2\Phi}{\partial\sigma_y\partial p_m} + \Delta\epsilon_v\frac{\partial^2\Phi}{\partial\sigma_y\partial\sigma_{eq}}\right) + \\
&\Delta\epsilon_d\frac{\partial^2\Phi}{\partial f\partial p_m}\left[An\frac{1}{(1-f)\sigma_y}(-p_m) + (1-f)\right]\Bigg\}
\end{aligned} \tag{A.7}$$

$$A_{21} = -\left[\frac{\partial\Phi}{\partial\sigma_y}\frac{\eta}{(1-f)\sigma_y}\sigma_{eq} + \frac{\partial\Phi}{\partial f}A_n\frac{1}{(1-f)\sigma_y}\sigma_{eq}\right] \tag{A.8}$$

$$A_{22} = -\left\{\frac{\partial\Phi}{\partial\sigma_y}\frac{\eta}{(1-f)\sigma_y}(-p_m) + \frac{\partial\Phi}{\partial f}\left[A_n\frac{1}{(1-f)\sigma_y}(-p_m) + (1-f)\right]\right\} \tag{A.9}$$

$$\begin{aligned}
B_1 = &\frac{1}{(1-f)\sigma_y}\left(\Delta\epsilon_d \underset{\sim}{n} - \frac{1}{3}\Delta\epsilon_v \underset{\sim}{I}\right) \times \\
&\left[\Delta\epsilon_d\left(\frac{\partial^2\Phi}{\partial\sigma_y\partial p_m}\eta + \frac{\partial^2\Phi}{\partial f\partial p_m}A_n\right) + \Delta\epsilon_v H\frac{\partial^2\Phi}{\partial\sigma_y\partial\sigma_{eq}}\right]
\end{aligned} \tag{A.10}$$

$$B_2 = \frac{\partial\Phi}{\partial\underset{\sim}{\sigma}} + \left(\frac{\partial\Phi}{\partial\sigma_y}\eta + \frac{\partial\Phi}{\partial f}A_n\right)\frac{1}{(1-f)\sigma_y}\left(\Delta\epsilon_d \underset{\sim}{n} - \frac{1}{3}\Delta\epsilon_v \underset{\sim}{I}\right) \tag{A.11}$$

$$G_1 = A_{11}^{-1} B_1 + A_{12}^{-1} B_2$$
$$G_2 = A_{21}^{-1} B_1 + A_{22}^{-1} B_2 \tag{A.12}$$

Appendix B. VAI application in a simple 1D problem

The inability of the standard Gauss integration scheme to integrate correctly the equilibrium equations in the case where all integration points are on the one side of the discontinuity can be shown by means of a simple 1D example:

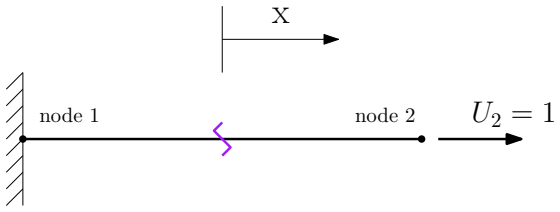

Figure B.35: 1D cracked bar model

We consider a bar of length $l = 1$, area $S = 1$, Young's modulus $E = 1$ and a $U_2^a = 1$ forced displacement on node 2 and a crack in the middle of the bar. The unknowns of the problem are U_i and U_i^*, the standard and additional degrees of freedom respectively of node i. A displacement is applied on node 2 ($U_2 = 1$), while node 1 is blocked ($U_1 = 0$). ($H(x+) = 0.5, H(x-) = -0.5, H_1 = -0.5$ and $H_2 = 0.5$)

$$N_1(x) = \frac{1-x}{2}, \quad N_1(x) = \frac{1+x}{2} \tag{B.1}$$

$$B' = B + B^* = \left[\frac{\partial N_1}{\partial x} \quad \frac{\partial N_1}{\partial x}(H(x) - H_1) \quad \frac{\partial N_2}{\partial x} \quad \frac{\partial N_2}{\partial x}(H(x) - H_2)\right] = \frac{1}{2}\left[-1 \quad -(H(x) + 0.5) \quad 1 \quad (H(x) - 0.5)\right] \tag{B.2}$$

$$B'^T \times B' = \begin{bmatrix} 1 & H+0.5 & -1 & -H+0.5 \\ H+0.5 & (H+0.5)^2 & -H-0.5 & -(H^2-0.5^2) \\ -1 & -H-0.5 & 1 & H-0.5 \\ -H+0.5 & -(H^2-0.5^2) & H-0.5 & (H-0.5)^2 \end{bmatrix} \tag{B.3}$$

where $H(x)$ has been replace by H for simplicity.

Using a 2 Gauss point rule with $x_1 = +0.577$, $x_2 = -0.577$ and $w_{1,2} = 1$, the stiffness matrix can be calculated using the following sum:

$$K = \sum_g [B'_g]^T [L][B'_g](Sw_g) \tag{B.4}$$

In this linear elastic case $[L]$ can be replaced by E. After manipulation of the equation and realizing the summation for the two GPs:

$$K = \frac{S\,E\,l}{2} \begin{bmatrix} 1 & 0.5 & -1 & 0.5 \\ 0.5 & 0.5 & -0.5 & 0 \\ -1 & -0.5 & 1 & -0.5 \\ 0.5 & 0 & -0.5 & 0.5 \end{bmatrix} \tag{B.5}$$

The displacements in nodes 1 and 2 are known, the forces contributions induced by the enriching dofs are zero and the unknowns of the problem are the displacements of the enriching dofs and the forces induced by the standard dofs.

$$\frac{1}{4} \begin{bmatrix} ... & ... & ... & ... \\ ... & K_{22} & ... & K_{24} \\ ... & ... & ... & ... \\ ... & K_{42} & ... & K_{44} \end{bmatrix} \begin{Bmatrix} U_1 = 0 \\ U_1^* \\ U_2 = 0 \\ U_2^* \end{Bmatrix} = \begin{Bmatrix} F_1 \\ F_1^* = 0 \\ F_2 \\ F_2^* = 0 \end{Bmatrix} \tag{B.6}$$

The determination of the enriching dofs displacements reduces to solving the

following system:

$$\frac{1}{4}\begin{bmatrix} K_{22} & K_{24} \\ K_{42} & K_{44} \end{bmatrix}\begin{Bmatrix} U_1^* \\ U_2^* \end{Bmatrix} = \begin{Bmatrix} 0 + U_1 K_{21} + U_2 K_{23} \\ 0 + U_1 K_{41} + U_2 K_{43} \end{Bmatrix} \Rightarrow \tag{B.7}$$

$$\begin{Bmatrix} U_1^* \\ U_2^* \end{Bmatrix} = \begin{Bmatrix} 1 \\ 1 \end{Bmatrix} \tag{B.8}$$

Finally, in order to obtain the displacement jump:

$$\begin{aligned} \{|U|\} = U^+ - U^- = \sum_{i=1}^{2} N_i(x^+)U_i + \sum_{j=1}^{2} N_j(x^+)U_j^* - \\ \sum_{i=1}^{2} N_i(x^-)U_i - \sum_{j=1}^{2} N_j(x^-)U_j^* = \\ = N_1(x^+)U_1^* + N_2(x^-)U_2^* = 1 \end{aligned} \tag{B.9}$$

where $N_1(x^+) = N_2(x^-) = 0.5$

After determining the displacement jump we then can proceed to calculate the cohesive tractions.

Using a 1 Gauss point rule with x=0 and w=2; considering that the crack is positioned in the middle of the bar but in the x+, we receive after manipulation of the equation:

$$K = \frac{S\,E\,l}{4}\frac{1}{2}w\begin{bmatrix} 1 & 1 & -1 & 0 \\ 1 & 1 & -1 & 0 \\ -1 & -1 & 1 & 0 \\ 0 & 0 & 0 & 0 \end{bmatrix} \tag{B.10}$$

The same procedure as above is followed:

$$\begin{Bmatrix} U_1^* \\ U_2^* \end{Bmatrix} = \begin{Bmatrix} 1 \\ NaN \end{Bmatrix} \tag{B.11}$$

Since the value of U_2^* is indeterminate, because the stiffness matrix is singular, it is not possible to determine one possible displacement jump and the respective cohesive tractions. In fact, all possible U_2^* values are admissible.

Application of VAI to the 1D bar problem.

Considering now the same case of 1 Gauss point rule we are going to apply the proposed VAI.

Using equation 49, where volumes have been replaced by lengths, the stiffness matrix of the finite element using VAI is expressed as follows:

$$K = \frac{l^-}{l}\sum_g [B'_g(H^-)]^T[L][B'_g(H^-)](Sw_g) + \frac{l^+}{l}\sum_g [B'_g(H^+)]^T[L][B'_g(H^+)](Sw_g) \quad \text{(B.12)}$$

The first sum considers that the integration point is on the 'negative' side of the crack ($H^- = H(x^-) = -0.5$) and the second sum considers that it is on the 'positive' side of the crack ($H^+ = H(x^+) = +0.5$). The crack being in the middle of the bar gives: $\frac{l^-}{l} = \frac{l^+}{l} = 0.5$.

$$K = \frac{S}{4}\frac{E}{2}\frac{l}{2}w\left(\frac{l^-}{l}\begin{bmatrix} 1 & 0 & -1 & 1 \\ 0 & 0 & 0 & 0 \\ -1 & 0 & 1 & -1 \\ 1 & 0 & -1 & 1 \end{bmatrix} + \frac{l^+}{l}\begin{bmatrix} 1 & 1 & -1 & 1 \\ 1 & 1 & -1 & 0 \\ -1 & -1 & 1 & 0 \\ 0 & 0 & 0 & 0 \end{bmatrix}\right) = \frac{S}{4}\frac{E}{2}\frac{l}{2}w\begin{bmatrix} 1 & 0.5 & -1 & 0.5 \\ 0.5 & 0.5 & -0.5 & 0 \\ -1 & -0.5 & 1 & -0.5 \\ 0.5 & 0 & -0.5 & 0.5 \end{bmatrix} \quad \text{(B.13)}$$

Using, then, equations B.6 and B.7 we are lead to:

$$\begin{Bmatrix} U_1^* \\ U_2^* \end{Bmatrix} = \begin{Bmatrix} 1 \\ 1 \end{Bmatrix} \quad \text{(B.14)}$$

This way it is evident that VAI can provide us with a correct displacement jump in the case of just 1 GP situated on one side of the crack, whereas the standard Gauss integration cannot.

Declaration of interests

☒ The authors declare that they have no known competing financial interests or personal relationships that could have appeared to influence the work reported in this paper.

☐The authors declare the following financial interests/personal relationships which may be considered as potential competing interests: